SALTATION OF PNEUMATICALLY CONVEYED NANOPARTICLES

by

SULEYMAN KEMAL BETIN

A thesis submitted to the

Graduate School-New Brunswick

Rutgers, The State University of New Jersey

in partial fulfillment of the requirements

for the degree of

Master of Science

Graduate Program in Mechanical & Aerospace Engineering

Written under the direction of

Prof. Jerry Shan

and approved by

_____

_____

_____

_____

New Brunswick, New Jersey

[January, 2008]

ABSTRACT OF THE THESIS

SALTATION OF PNEUMATICALLY CONVEYED NANOPARTICLES

by Suleyman Kemal Betin

Thesis Director: Prof. Jerry Shan

The saltation velocity, the air velocity at which particles start to settle and form dunes and layers during their pneumatic transport, is experimentally studied for nano-particle aerosol in a horizontal pipe. The nano-particles used are silica with primary particle size of 30nm and agglomerate size of 200-300nm and carbon black with average size of 45 nm. The nano-particle aerosol is characterized using DMA. The saltation of nano-particle aerosol is compared qualitatively with that of glass beads and quantitatively with the predicted values of Matsumoto correlation, which is verified for 47.5 μm glass beads. The saltation of nano-particle aerosols was different than that of 47.5 μm glass beads in terms of the form and the initial position of the particles that settle. The saltation Froude numbers predicted by Matsumoto are an order of magnitude higher than the experimental results for nano-particles and the discrepancy is explained by comparing the external forces acting on a particle through its interaction with another particle. The saltation of the silica nano-particles was different than that of carbon black nano-particles: the saltation Froude number was essentially independent of mass loading ratio for nano-silica. The difference in the saltation behavior of two nano-particle aerosols is explained by particle charge measurements and control volume analysis.

Acknowledgement

I would like to thank my advisor Prof. Shan for his invaluable guidance for my thesis. I feel lucky to have the chance to work with him, as I believe that this experience has taught me not only to become a better experimentalist and an engineer but also become a better person. I will always remember his support, positive attitude, dedication, professionalism and sense of humor.

I would also like to thank to Prof. Tse for providing space in his lab, access to the plasma lab, lending parts and fittings and also giving me permission to use DMA which is crucial equipment in my research.

Thanks to Dr. Ganesh Skandan and NEI for the purchase of the nano-powders and also the key components like aerosol generator and electrical field detector.

I owe a lot to Mr. John Petrowski for his unlimited help in the machine shop, for numerous parts and tools I borrowed from him, for his interest in Turkish language and all the great conversations we had. I will always remember him as the most easy going, skillful and helpful person in the department.

Thanks to the support of my parents, my sister, brother in law, my uncle and my auntie who always prayed for my success.

I have to admit that I was able to finish this research with the spiritual help of Rebecca Blankinship. She put up with my frustration and supported me with incredible love, patience and faith from the end to the beginning. She helped me to believe in myself and gave me the greatest strength to keep on going in this long and tough journey.

Dedication

I dedicate this work to my family and to Rebecca.

Table of Contents

List of Figures

Chapter 1

Introduction

In the horizontal pneumatic conveying of particles, it is desirable to operate at as low an air flow rate as possible to minimize the energy consumption, particle attrition and pipe wear. However, if the conveying air velocity is reduced past a certain value, unstable operation and the blockage of the pipe can result. The terms saltation velocity, critical velocity and minimum-transport velocity are most commonly used to refer to this air velocity. Definitions of these terms are based on visual observations and pressure-drop measurements.

The pneumatic conveying of particles can be represented by a Zenz type plot as shown in Fig. 1.

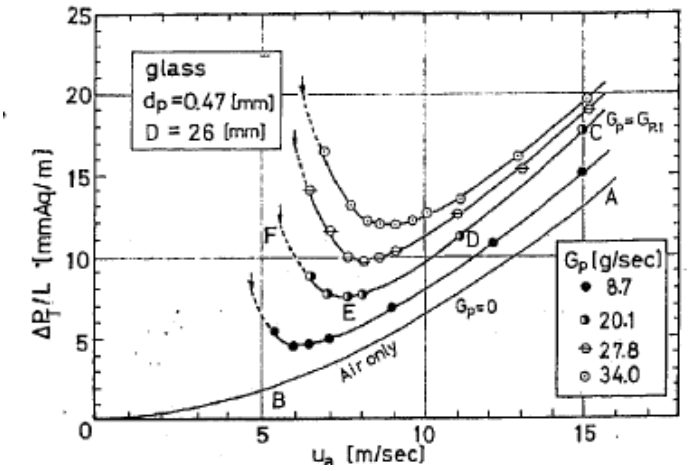

Figure 1: Relations between pressure drop and air velocity with parameter of solids flow rate [1].

Curve AB is the pressure drop for particle-free air, while the other curves are for particle-laden flow with constant feed rate of particles (Gp).When the superficial air

velocity is reduced from the value at point C to that at point D, for a constant solids rate Gp, the pressure drop decreases. In this case, the particles are air borne, distributed uniformly in the pipe. When the gas velocity is reduced further from that at point D, the particle concentration at the bottom of the pipe increases, and the flow becomes heterogeneous. The pressure drop per unit length shows a minimum value when the conveying-air velocity is reduced to point E. According to the visual observations of Matsumoto's first study [1], at this point, almost all the particles slide on the bottom, although a settled layer has not yet appeared. The air velocity at this pressure minimum point is defined as the saltation velocity.

If the gas velocity is further reduced from point E to point F, the pressure drop increases rapidly. At point F, the particles begin to settle on the bottom of the pipe and a stationary bed is formed. The air velocity at this point is called the minimum transport velocity. The dashed line between point E and F implies an unsteady transition region between the saltation velocity and minimum-transport velocity although this is not clearly reported**.**

Wirth [2] describes similar flow patterns and pressure-drop measurements in more detail. However, he defines the air velocity at which pressure-drop measurements become unsteady as the critical velocity. At the critical velocity, the dunes and layers are formed and, because the pipe cross-section is decreased, the air velocity increases, causing the pressure-drop measurements to fluctuate. The pressure-drop measurements associated with the flow patterns are shown below.

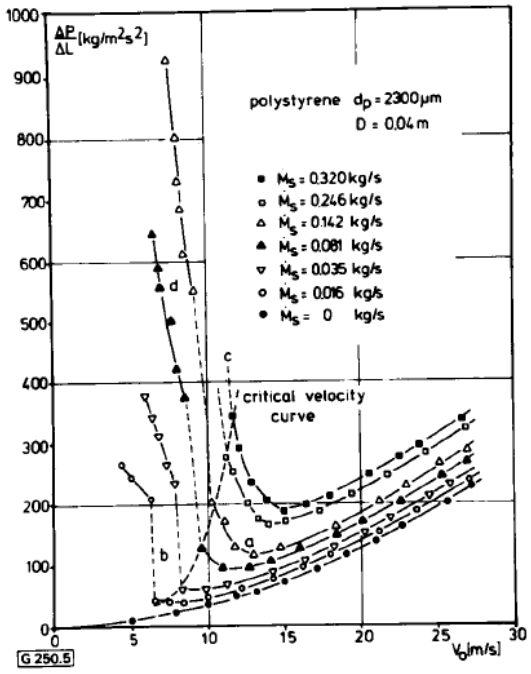

Figure 2: Measured critical velocities for conveying of polystyrene particles in a glass pipe; a) Strand-type conveying and fully suspended flow; b) dune flow; c) plug flow ; d) conveying over a settled layer. Wirth [2] (1980)

As seen from the figure above, for higher mass loading ratios, the value of saltation velocity is greater than the critical velocity, which in turn is larger than minimum-transport velocity. However, as the mass feed rate is reduced, these three different velocities become equal to each other, a fact that was also reported by Matsumoto. It is believed that the value of the particle-mass-feed rate at which the three different velocities collapse depends on the particle density, particle diameter and pipe diameter.

There are numerous correlations in the literature that predict the velocities mentioned above which are based on experiments done with millimeter- and micrometer-sized particles.

Matsumoto in his first study about saltation velocity, used glass, copper and polystyrene particles with sizes ranging from 300 μm to 2100 μm in pipes with inner diameters of 20 mm and 49 mm. He found the following correlation:

$$Fr = 13.1\left(\frac{\rho_p}{\rho_f}\right)^{-0.17}\left(\frac{Fr_p}{10}\right)^{0.58} m^{0.33} \qquad (2.1)$$

where Fr is the Froude number based on saltation velocity, and *m* is the mass loading ratio, a measure of concentration defined as the ratio of the particle-feed rate and mass-flow rate of air.

In his third paper, Matsumoto [3] studied the saltation of glass beads and copper particles for a wide range of sizes (20 μm and 1640 μm) The particle-size range was classified into fine and coarse based on a critical diameter (dp*) which was calculated from the equation

$$\frac{d_p^*}{D} = 1.39\left(\frac{\rho_p}{\rho_f}\right)^{-0.74} \qquad (2.2)$$

The correlations for fine and coarse particles are shown in the following equations.

For dp < dp* (fine particles)

$$m = 5.56 * 10^3\left(\frac{d_p}{D}\right)^{1.43}\left(\frac{Fr}{10}\right)^4 \qquad (2.3)$$

For dp* < dp (coarse particles)

$$m = 0.373 * 10^3\left(\frac{\rho_p}{\rho_f}\right)^{1.06}\left(\frac{Fr_p}{10}\right)^{-3.7}\left(\frac{Fr}{10}\right)^{3.61} \qquad (2.4)$$

Wirth [2] studied the critical velocity of silica sand, glass beads and polystyrene particles for a size range of 90 μm to 2300 μm in pipes with inner diameters of 10 mm and 40 mm. Based on his experiments, he reported the following correlation:

$$Fr = 2.730\left((1-\varepsilon) C_f r^2 \left(\frac{\rho_p{}^2 + \rho_f{}^2}{\rho_p \rho_f} + 2 \right) m \right)^{1/4} \qquad (2.5)$$

where C_f is the coefficient of sliding friction and ε is the void fraction. Values of these coefficients must be known or assumed in order to calculate the saltation velocity.

Gunther's [4] correlation is based on the boundary-layer theory of Schlichting with constants correlated using data on wheat.

$$Fr = \left(\frac{B_s{}^2}{\left(D/d_p\right)^{5/7}\left(1+m^{1/2}\right)} + A_s{}^2 m^{1/2} \right)^{1/2} \qquad (2.6)$$

For wheat, the coefficients A_s and B_s were 10.0 and 23.4, respectively.

Rizk [5] used his experimental data on styropor and polystrol with a size range of 731 μm and 5650 μm for pipes with inner diameters of 49.6 mm and 52.6 mm to find the correlation:

$$Fr = \left(10^{\delta} m\right)^{1/\chi} \qquad (2.7)$$

where $\delta = 1.44 d_p + 1.96$ and $\chi = 1.1 d_p + 2.5$ for which d is in mm

Plasynski [6] reviewed the correlations in the literature by assuming that the saltation, critical and minimum transport velocities are numerically equal. The correlations of Wirth [2], Gunther [4] and Rizk [5], and the correlation from the third paper of Matsomoto, were concluded to give better predictions than the others. On an overall basis, Matsomoto's correlation was recommended since it yields the lowest root

mean square (R.M.S) of the deviations of the predicted Froude numbers from all of the available experimental data; this RMS deviation was 25% for Matsumoto.

All of the existing correlations in the literature are based on experiments done with micron-sized or millimeter-sized particles. To our knowledge, there has not been a study of the horizontal pneumatic transport of a nano-particle aerosol in regards to settling and blockage.

The deposition of nano-particles in bifurcating tubes, in upper bronchial airways and in cylindrical pipes has been studied numerically by Shi *et al* [7], experimentally by Cohen [8] and analytically by Ingham [9] and Martonen [10]. Similarly, the re-entrainment of nano-particles from surfaces to turbulent flows is another phenomenon that was investigated experimentally by several authors like Otani [11], Wen and Kasper [12] and Wen *et al* [13].

In this study, we experimentally investigate the air velocity at which a nano-particle aerosol starts to form dunes and layers during its pneumatic transport in a horizontal pipe. The saltation Froude numbers of micron-sized glass beads were measured and compared with the predictions of the various well-known correlations. The tests were repeated for carbon-black and silica nano-particles and the flow patterns were observed. We explain the difference between the results of the carbon black and silica with the help of the indirectly measured charge levels of the aerosols. Finally, the saltation Froude numbers of the nano-particle aerosols were compared with the predicted values of the Matsumoto correlation.

Chapter 2

Experimental Apparatus

The schematic of the experimental set-up used for this study is shown in Fig 1.

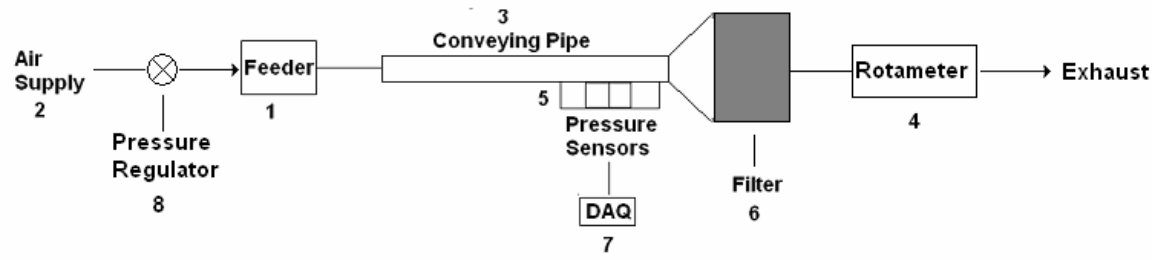

Figure 3: The schematic of the experimental apparatus

The feeder used was a SAG 410/H high flow rate aerosol generator (Topas-Gmbh). This feeder creates the aerosol by utilizing a dry dispersion technique which picks up and disperses the particles through a venturi nozzle. One of the main reasons that this feeder was selected is that it can disperse particles down to 100 nm size. The other reason is that its particle mass-feed-rate is high enough to approach the mass-loading ratios common in the literature, specifically in Matsumoto (1977) [3]

For micron-sized particles, spherical glass beads (Potters Industries, Inc.) were used since they are the most commonly used particles in the literature. By using a COULTER LS Particle Size Analyzer, their mean diameter and coefficient of variation were measured to be 47.5 μm and 0.34 respectively.

For nano-particles, silica particles (Cabot Technologies) with primary particle size of 30nm and agglomerate size of 200-300nm were used. Since electrostatic forces associated with nano-particles are considered to be significant, in order to investigate the

effect of particle charge, conducting carbon black particles (Alfa Aesar Corp) with an average size of 45 nm were used. To further increase the range of mass loading ratios, and also to investigate the effect of bulk density, carbon-black powders with different bulk densities, namely 50%- and 100%- compressed carbon black were used.

In order to understand how well the SAG 410/H dispersed the nano-particles that were used, the silica and carbon-black aerosols were sampled iso-kinetically and their size distribution was measured by a SMPS system with long DMA (TSI Inc.). The details of the measurement are provided in Appendix E. A lognormal curve fit is used in order to determine the count mean, standard deviation and mass mean diameter. The formula used to determine mass-averaged mean diameter is:

$MMD = \frac{\sum m_i d_i}{M} = \frac{\sum n_i d_i^{\,4}}{\sum n_i d_i^{\,3}}$ [14], where m_i , d_i and n_i are the mass, diameter and number of particles respectively and M is the total mass. The results are shown in the following figures.

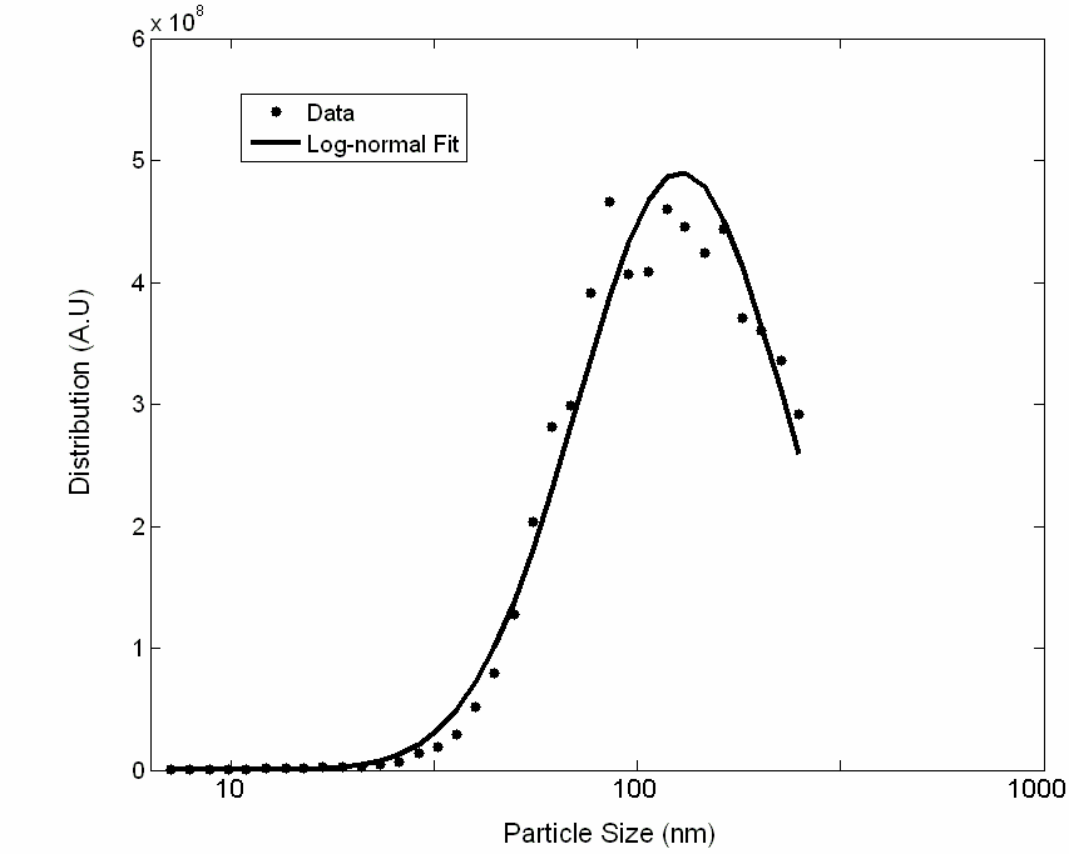

Figure 4: The size distribution of the carbon-black 50% aerosol. The lognormal fit yields a count mean of 127 nm, mass mean diameter of 351 nm and a geometric standard deviation of 1.89 nm.

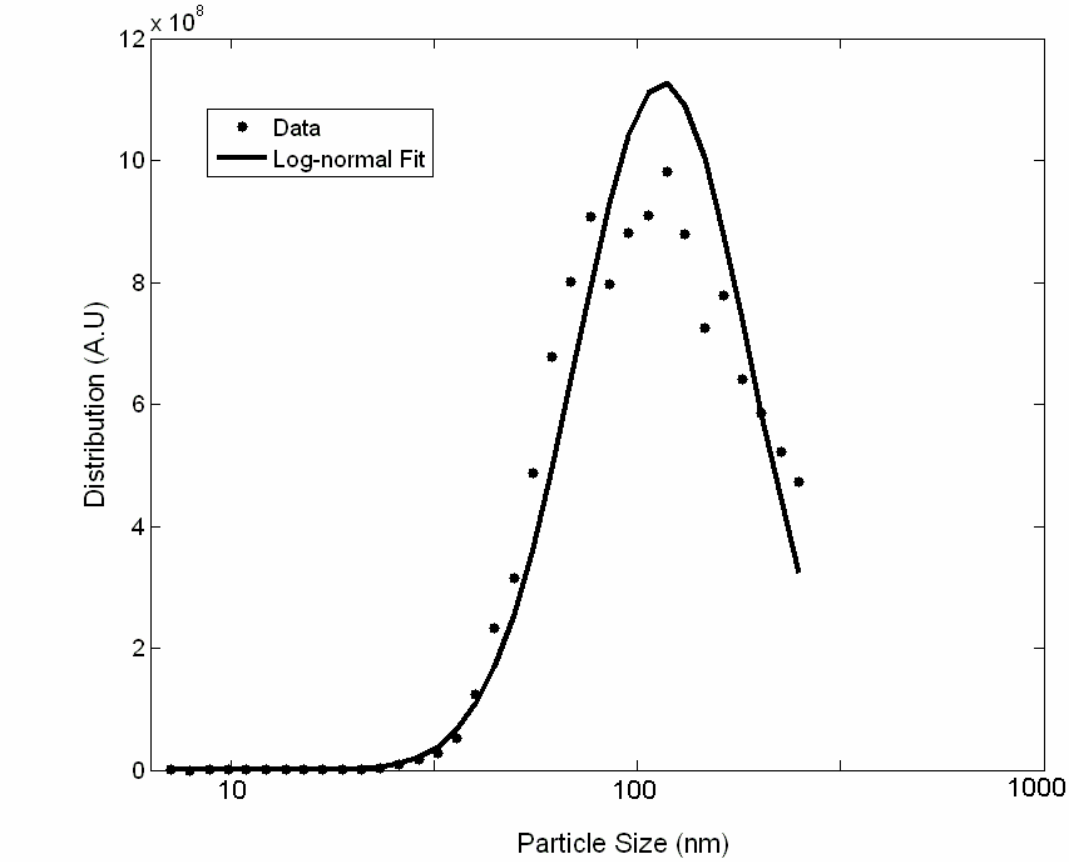

Figure 5: The size distribution of the carbon black 100% aerosol. The lognormal fit yields a count mean of 114 nm, mass mean diameter of 202 nm and a geometric standard deviation of 1.61 nm.

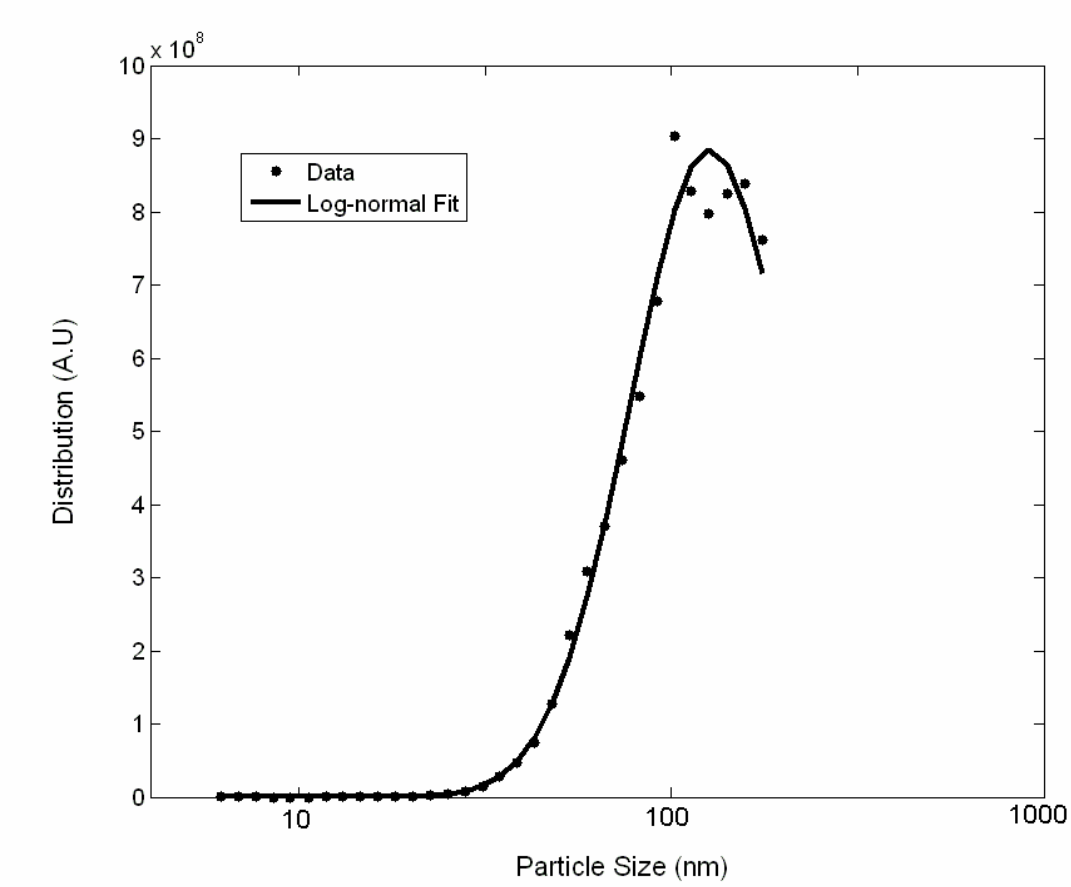

Figure 6: The size distribution of the silica aerosol. The lognormal fit yields a count mean of 114 nm, mass mean diameter of 288 nm and a geometric standard deviation of 1.74 nm.

From the figures above, it is clearly seen that SAG 410/H can disperse and generate an aerosol of nano-particles. Mass-averaged mean diameters of 200 and 350 nm were found for 100%- and 50%- compressed-carbon-black aerosols, respectively, while the silica aerosol had a mass-averaged mean diameter of 290 nm.

For the aerosol conveying pipe, two drawn-aluminum pipes with inner diameters of 0.82 in. and 1.05 in. were used for micron-sized glass beads. The pipe diameters were chosen so that settling occurred with the available mass-feed-rate and air-flow-rate ranges for the glass beads. Additionally, the flow patterns are observed visually, by using a clear PVC pipe of 1.02 in. inner diameter. To account for the pressure-drop-measurement

length and also for the acceleration length of the two-phase flow, 20-foot long pipes were used.

Five pressure taps are placed with three-foot intervals along the test pipes to detect particle settling and dune formation. The interval length is based on the sensitivity of the pressure transducers and on Hinkle's correlation [14] which predicts the pressure drop of a two-phase flow in horizontal pipes. To account for the distance to achieve fully developed particle laden flow, the pressure gradients were measured at a section more than 7.5 feet distant from the feeding point of the particles. A set of pressure transducers with an accuracy of 0.05 in H20 was used to measure the differential pressure between tap locations along the pipes.

The pressure drop of the two-phase flow was found to be linear within the limits of the transducers. Therefore, the two-phase flow was believed to be fully developed at the measurement location (> 7.5 feet from the pipe entrance).

For nano-particles, settling occurred in pipes with nominal diameters of 1.5 in. and 2 in.. However, as the mass feed rate and the air velocity during settling was low, it was difficult to detect the instability in the pressure drop for test runs of reasonable duration. Therefore, the settling was observed visually by using clear PVC pipes of 40.44 mm (1.59 in.) and 51.51 mm (2.03 in.) inner diameters.

The air flow rate is measured with a rotameter from King Instrument Company with a range of 0-20 standard cubic feet per minute and an accuracy of 2% of full scale.

Chapter 3

Results and Discussion

3.1 Saltation Velocity of Glass Beads

Firstly, the saltation of 47.5 μm glass beads was studied to develop the experimental procedure and validate existing correlations in the literature. For the micron-sized glass beads that were conveyed in aluminum pipes, the experiments were carried out by reducing the air flow rate (for a constant solids flow rate) until the pressure-drop measurements became unsteady. For the ones conveyed in PVC pipes, both pressure measurements and visual observations were utilized.

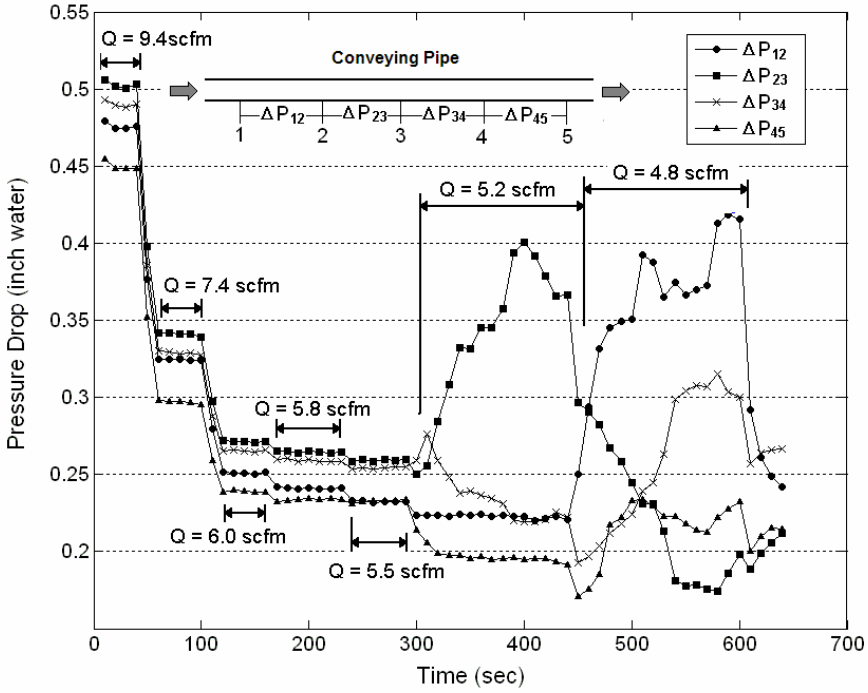

Figure 7: Representative pressure trace for the saltation velocity of micron-sized glass beads in aluminum pipe.

Figure 7 shows the pressure drop measured in 0.82 in. inner-diameter aluminum pipe at a glass-bead feed rate of 165 g/min. The pressure drop decreases with each reduction in the flow rate (Q) until a certain value is reached. At 147 lpm (5.2 scfm), the pressure drop ΔP_{23} increases, indicating that there is a restriction in the pipe cross section due the formation of a layer or dune between the pressure taps 2 and 3. This restriction leads to an increase in the conveying air velocity and therefore an increase in the pressure drop at that location.

Visual observations together with pressure measurements in PVC pipes also revealed that as the dunes formed, unsteady pressure-drop measurements were recorded at those specific locations. As can be seen from Fig. 8, a dune formed between the pressure taps 2 and 3 in 1.02 in. I.D PVC pipe. The picture of the dune is shown in Fig. 9.

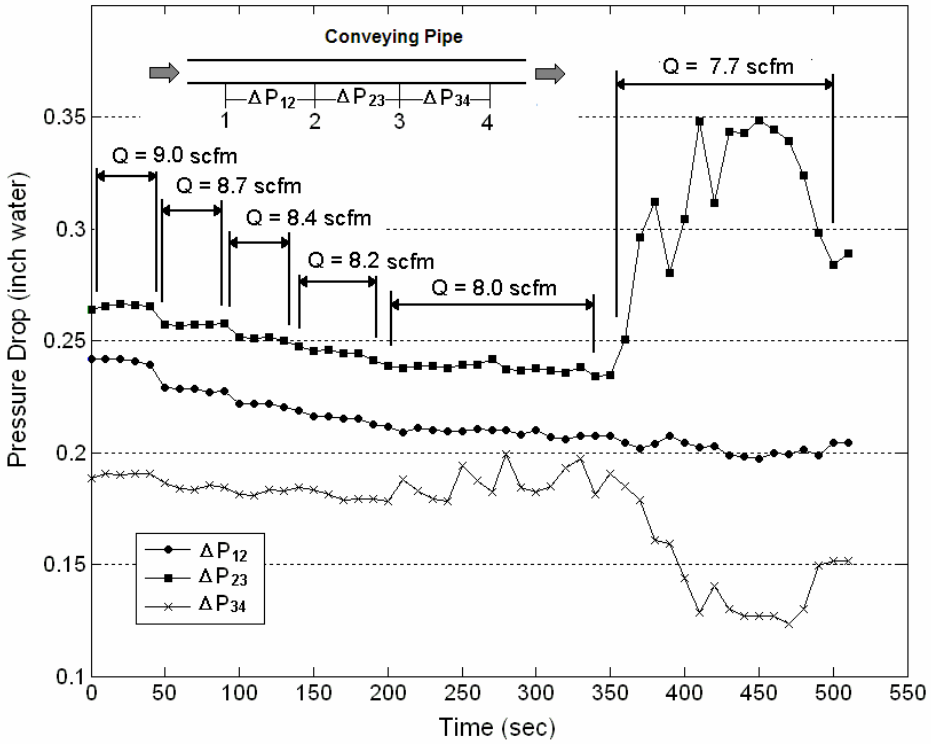

Figure 8: Pressure measurements in the PVC pipe.

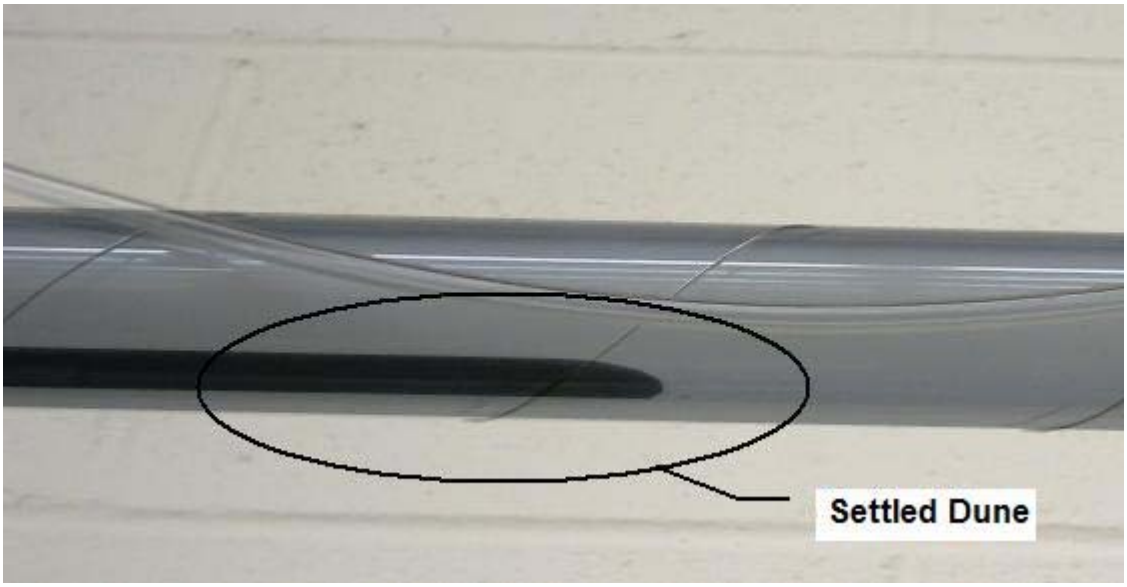

Figure 9: The settled dune of glass beads between pressure taps 2 and 3 in the PVC pipe. A wire is wrapped around the pipe to minimize the electrostatic effect on the pressure sensors.

Measurements of the saltation velocity were made for varying mass-flow rates. The data were presented in dimensionless form by non-dimensionalizing the saltation velocity and particle mass feed rate as the Froude number, Fr , and mass-loading ratio, m , respectively.

The formula for mass loading ratio is: $m = \frac{\dot{m}_s}{\dot{m}_a}$, where $\dot{m}_s$ and $\dot{m}_a$ are the mass feed rate of particles and mass flow rate of air, respectively.

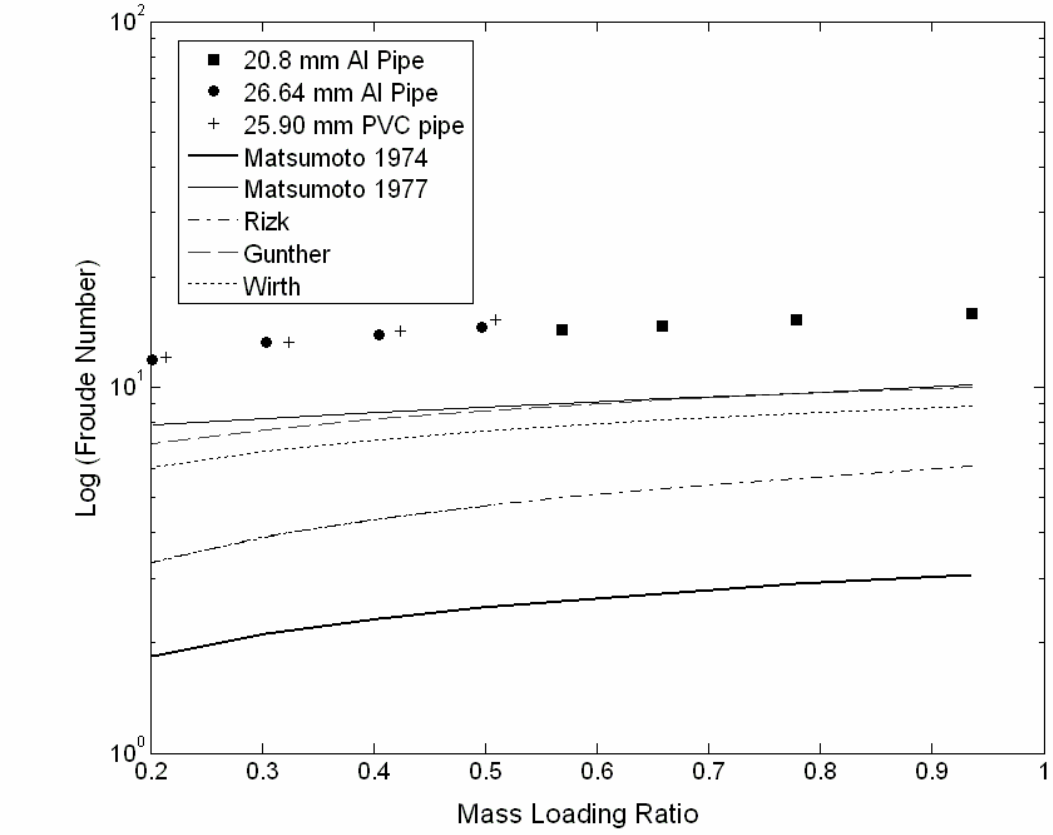

Figure 10: Comparison of experimental values with well known published correlations

Figure 10 shows a comparison of experimental values with the well known correlations discussed previously. As it can be seen from the figure, the correlations of Matsumoto 1977 [3], Gunther [4] and Wirth [2] agreed better with the experimental results than those of Rizk [5] and Matsumoto 1974 [1]. For Günther's correlation, the constants *A* and *B* were assumed to be those for wheat which were 10.0 and 23.4, respectively, in the absence of any other information. Also, for Wirth's correlation, the values of the coefficient of sliding friction and the void fraction were assumed to be 0.3 and 0.4, respectively. Since the accuracy of the Günther [4] and Wirth [2] correlations

rely on the values assumed for their constants and coefficients, it is concluded that the Matsumoto 1977 [3] correlation gives the best prediction for glass beads.

Qualitatively, the trend of the experimental data agreed with the correlations in the sense that Froude number increases with increasing mass loading ratio. Quantitatively, the discrepancy between the predicted values of Matsumoto 1977 [3] and the measured experimental values was 39.8% in terms of the root-mean-square of deviations (R.M.S of deviation) of the Froude numbers. Although this appears to be high, it is consistent with the 25% discrepancy between all of the available data and the Matsumoto 1977 [3] correlation that was found by Plasynski [6].

3.2 Saltation Velocity of Nanoparticles

After observing the settling of micron sized glass beads and concluding that Matsumoto 1977 [3] predicts the saltation Froude number reasonably well, the tests were repeated for three different nano-particle aerosols (silica, 50% compressed carbon black and 100% compressed carbon black) and the flow patterns were observed in clear PVC pipes. Due to the low mass-loading ratios of the aerosol, layers and dunes built up slowly at saltation. Very long operation times were needed to detect a resultant change in the pressure and this meant consumption of nano-particles in unreasonable amounts. Since it was previously verified with the glass beads that the pressure measurements and visual observations of dune formation gave the same results, only visual observations were utilized for the nano-particles.

For all three nano-particle aerosols, although the aerosol entering the pipe was well dispersed and contained nano-particles (Figs. 4, 5 and 6) large agglomerates of nano-particles with irregular shapes were observed to slide and bounce along the bottom of the pipe, starting from the point approximately 60 cm (2 feet) distant from the entrance, to the end of the pipe. From analysis of the pictures taken, the size of these agglomerates reached up to millimeter range (Fig. 11). When the air flow rate was reduced to a certain value, these nano-particle agglomerates stopped sliding or bouncing and formed settled layers and dunes.

This settling of nano-particle aerosols was different than the one that was observed in the experiments with 47.5 μm glass beads in two aspects: the form and the initial position of the particles that settle. For the glass beads, the settling particles were the individual beads themselves which were suspended in the conveying air before settling. Once the air-flow rate reached a certain value, these particles dropped out of suspension and immediately formed settled dunes and layers. However for nano-particles, the settling particles were in the form of large nano-particle agglomerates sliding and bouncing along the bottom of the pipe and these agglomerates were not airborne immediately before saltation.

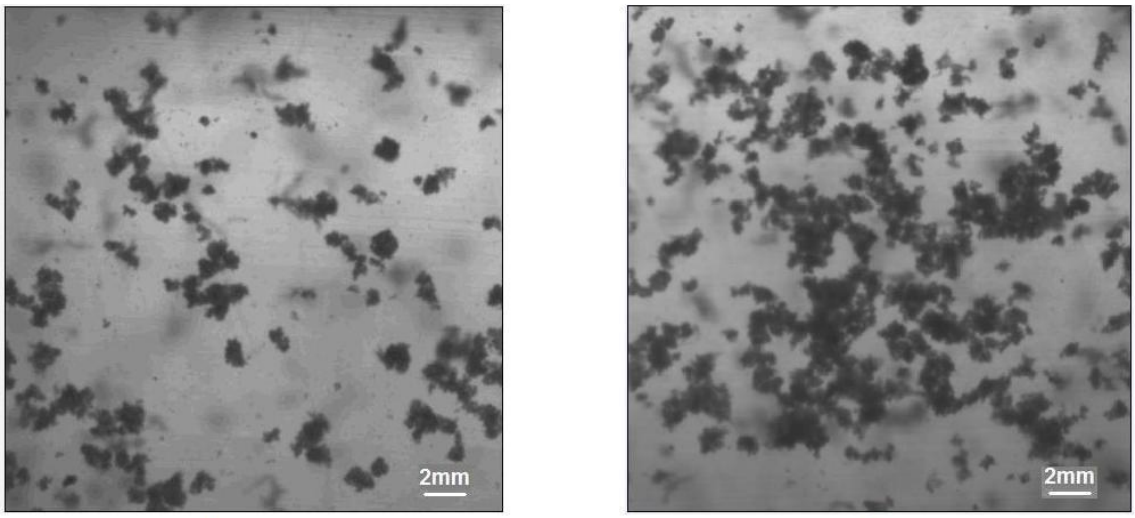

Figure 11: Large agglomerates of silica nano-particles traveling at the bottom of a 25.9mm (1.02 in.) I.D PVC pipe at a mass feed rate of A) 2.98gr/min. B) 4.86gr/min.

As can be seen from the pictures above, as the particle mass-feed rate (therefore the mass-loading ratio) was increased, the number of agglomerates traveling at the bottom of the pipe increased. The size of the agglomerates may have also increased. However, it is not possible to quantify the mean size due to substantial overlap in the high concentration image (Appendix C).

The measured saltation Froude numbers and mass-loading ratios are plotted in Fig. 12 for carbon-black and silica nano-particles. The Froude number is based on the air velocity at which the nano-particle agglomerates settle.

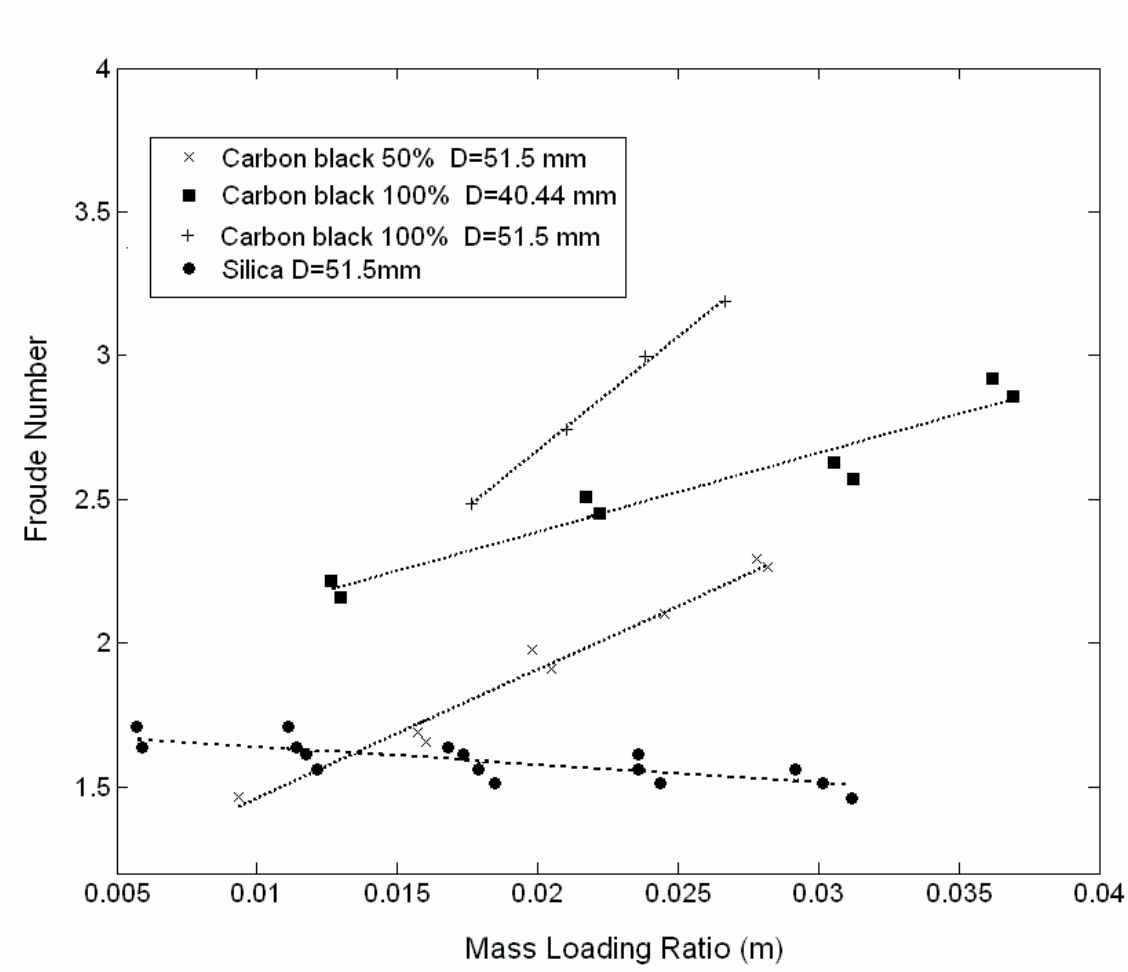

Figure 12: Saltation Froude number and mass loading ratio for Silica, Carbon Black 50% and Carbon Black 100% particles.

For carbon-black nano-particles, the saltation Froude number increased with increasing mass loading ratio, as typically observed in studies of micron-sized and larger particles (Fig 10). However, a striking difference can be seen between the saltation behavior of nano-particle silica, and that of carbon black, micron-sized glass beads and other particles reported in the literature. As can be seen from the above figure, the saltation Froude number of nano-silica was independent of (or even slightly decreasing with) mass loading ratio. We will return to the discussion of this unusual behavior of silica nano-particle aerosal later in the paper.

In order to compare the experimental results with the values predicted by the Matsumoto 1977 [3] correlation, and to test its validity for nano-particle aerosals, the particle-size parameter, d_p, must be known. Two values were considered for this parameter: the count-mean diameter of the nano-particle aerosols, CMD = 114 nm, and the mass-mean diameter, MMD = 351 nm. The predicted saltation Froude number can then be calculated from the Matsumoto 1977 [3] and compared to the experimental values, as shown in the Fig. 13 below.

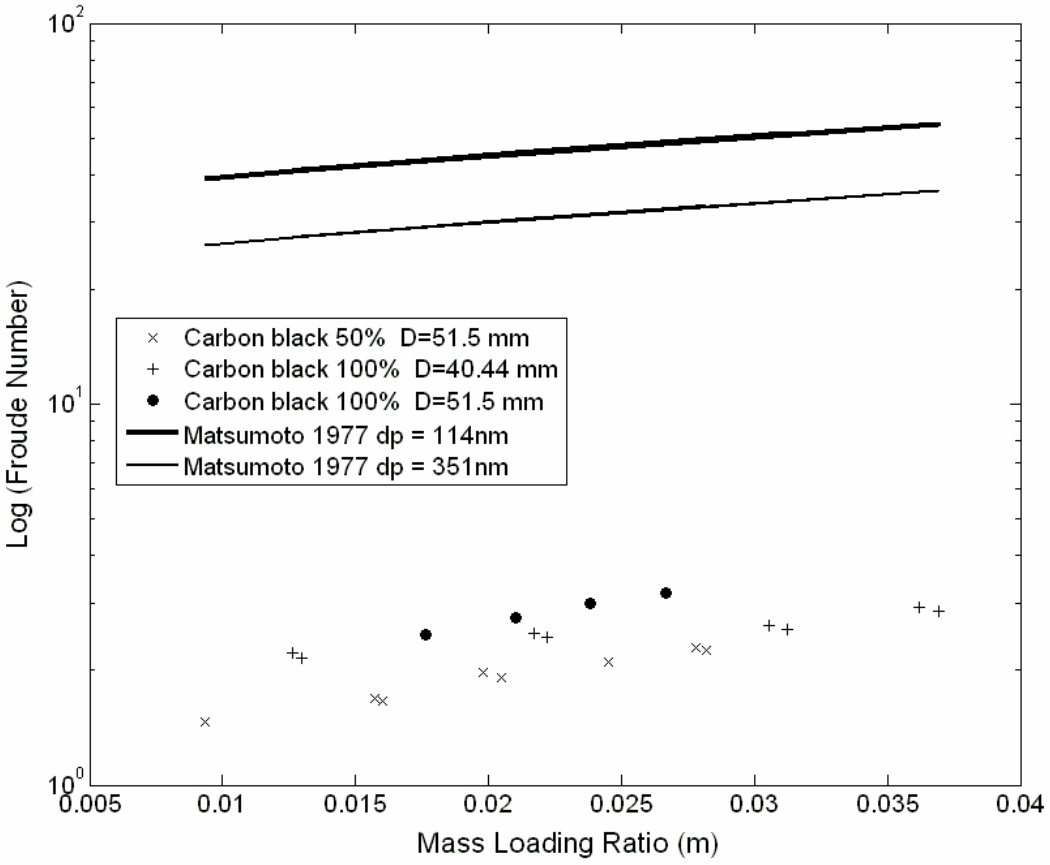

Figure 13: Comparison of Matsumoto 1977 [3] correlation with the experimental results for carbon and silica nano-particles.

As can be seen from the picture, for both values of particle size, the saltation Froude numbers predicted by Matsumoto 1977 [3] are an order of magnitude higher than the experimental results. However, it can be shown that this very comparison is not reasonable since the particles are nanoparticles and Matsumoto (1977 [3]) is based on Froude number. The reason is clear once the external forces acting on the particles as function of their sizes are calculated.

We consider the magnitudes of the gravitational, thermal, electrostatic and Van Der Waals (VDW) between two particles. To calculate the latter two, a characteristic length scale must be taken for the particles. Two values are considered for this length scale. The first one, x_1, is taken to be the distance between uniformly spaced particles in the aerosol and the second one is taken to be the diameter of the particle, $x_2 = d_p$

x_1 is based on the following derivation with the assumption that the particles are uniformly distributed:

Therefore the particle number concentration is: $\frac{\dot{\#}}{\dot{Q}} = \frac{m * \rho_f}{\frac{1}{6}\pi * {d_p}^3 * \rho_p}$ where $\dot{\#}$ is the number feed rate of particles, $\dot{Q}$ is the air flow rate, ρ_f is the conveying air density, ρ_p is the particle density and d_p is the particle diameter.

The cubic root of the reciprocal of $\frac{\dot{\#}}{\dot{Q}}$ yields the separation distance for uniformly distributed particles,

$$x_1 = \left(\frac{\frac{1}{6}\pi * {d_p}^3 * \rho_p}{\rho_f} \frac{1}{m} \right)^{1/3} \qquad (4.8)$$

We have chosen m to be 0.066 ,which is the maximum mass-loading-ratio value used in the experiments.

We note that x_1 is consistently higher than x_2. For the electrostatic and VDW forces, the calculated values based on x_1 and x_2 are considered to represent the case of uniformly distributed particles (a lower limit on the force) and the case of particles approaching contact, respectively.

Additionally, the charge of the particles was assumed to be the average Boltzmann-equilibrium charge which is based on the formula $q \approx 2.37\sqrt{d_p}$ [15], where d_p is particle size in μm. The average charge and therefore electrostatic force are calculated without regard to sign, *i.e*. repulsion or attraction. For particles below 100 nm when the formula would yield fractional charge on particles, the charge is taken to be unity. The average Boltzmann-equilibrium charge represents the average charge that a monodisperse aerosol has after it is subjected to neutralization. Thus, it is in some sense a lower limit on the particle-charge level. Therefore the calculated electrostatic force in this case is much lower than it would be if the particles were highly charged. However, these calculations are still useful in giving a lower limit on the electrostatic forces between particles.

For the gravitational force, the particle density was taken to be that of carbon black, which is 2000kg/m^3. The thermal force F_T is based on the Stokes -Einstein derivation [16].

$$F_T = \frac{3\pi * \mu * V_p * d_p}{C_c} \qquad (4.9)$$

where μ is the viscosity, V_p particle mean thermal velocity, and C_c is the Cunningham correction factor.

The following formula is used for the electrostatic, $F_{E,n}$, force:

$$F_{E,n} = \frac{K * q^2}{x_n^{\ 2}} \qquad (4.10)$$

where q is the charge of the particle [17].

The VDW force which can be derived from the potential-energy equation of two spherical surfaces:

$$F_{VDW,n} = \left(-\frac{H}{12 d_p} \right) * \left(-\frac{2(\alpha_n + 1)}{\left((\alpha_n + 1)^2 - 1\right)^2} - \frac{2}{(\alpha_n + 1)^3} + \frac{4}{(\alpha_n + 1)^3 \left(1 - \frac{1}{(\alpha_n + 1)^2} \right)} \right) \qquad (4.11)$$

where $\alpha_n = \frac{x_n}{d_p}$ [18].

The calculated forces as a function of particle size are shown in Fig. 14.

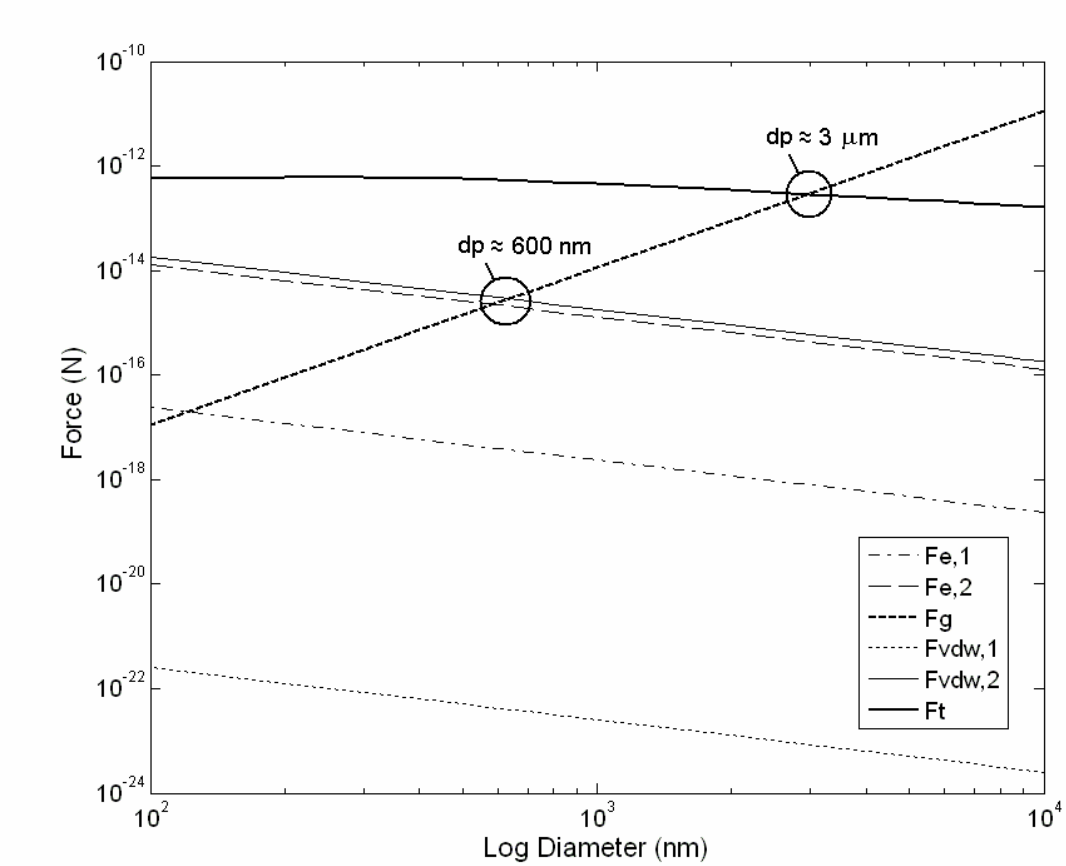

Figure 14: Comparison of external forces acting on a single particle.

We first consider the electrostatic and VDW forces. As can be seen from the figure, VDW forces only become significant when the particles come near contact; for the characteristic length, x_1, $F_{VDW,1}$ is negligible. For particles approaching contact, $F_{VDW,2}$ becomes significant compared to the gravitational force for a particle size of 600nm and below. As mentioned before, the average Boltzman equilibrium charge values used in the calculations underestimate the electrostatic forces. However, for particles near contact, the electrostatic forces become greater than the gravitational force also around 600nm, even for "neutralized" nano-particles. Thus, they can be expected to be significant, especially for highly charged nano-particles.

However, once the thermal force is considered, it can be seen that for particle size less than 3 μm, the thermal force becomes larger than the gravitational force. Therefore the Froude number, which only considers gravitational and inertial force can not completely characterize the saltation of particles smaller than roughly 3 μm. For this reason, it is not reasonable to expect the Matsumoto (1977 [3]) correlation, which is based on Froude number, to hold for nano-meter sized particles.

We now return to the unusual saltation behavior of the silica nano-particles, in which the saltation velocity was essentially independent of mass loading. To understand this, we consider the electrostatic forces acting on the particles. The charge levels of the silica nano-particles entering and exiting the pipe were measured by introducing the aerosol into a HEPA filter and measuring the electrical field resulting from the accumulation of the charged particles on the surface of the filter. For silica, the measured electrical field was -1500 kV/m, at a distance of 3 cm. This did not change regardless of whether the particles were measured at the entrance of the pipe or the exit of the pipe. In contrast, for carbon-black-nano-particle aerosol, the measured electrical field was essentially zero (fluctuating between +5 kV/m and -5 kV/m) for the same conditions. This indicates that silica nano-particles had a much higher charge than carbon black nano-particles did. The origin of the charge was further investigated by measuring the electrical field of the silica resting in the vessel of the feeder; this was found to be -50 kV/m, which is negligible compared to -1500 kV/m. Based on this, it is believed that silica nano-particles acquire their high charge when they are dispersed by the stainless steel nozzle of SAG 410/H. The observed negative polarity of the charge acquired by

silica through its contact electrification with stainless steel was also consistent with the data reported by Lowell [19].

It is believed that, the negatively charged silica nano-particle agglomerates are held together with Van der Waals forces in their agglomerated form, and they retain at least some of the negative charge of the individual particles. The surface of the conveying PVC pipe can also be negatively charged, either through collisions with negatively charged particles or the deposition of a thin layer of charged nano-particles. Therefore the electrostatic-repulsion forces between the highly charged silica agglomerates and the pipe surface can change the force balance and effect the saltation.

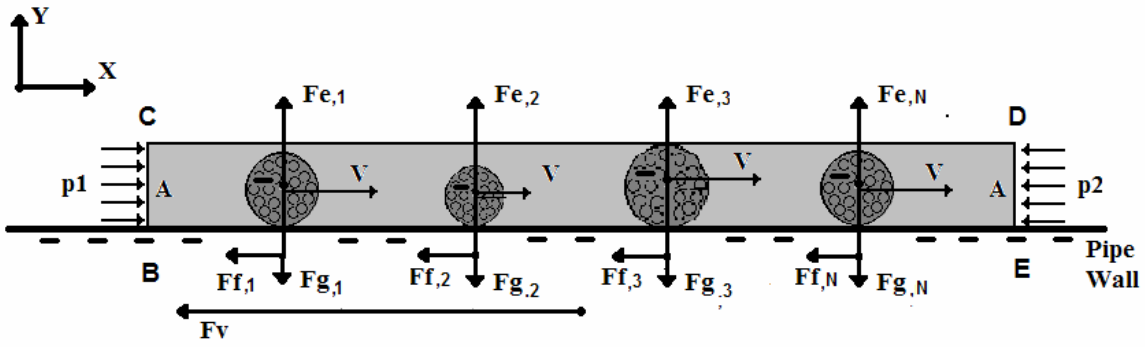

Figure 15: Force balance on a control volume containing the agglomerates.

To show this, we consider a control volume BCDE that only contains the agglomerates sliding at the bottom of the pipe at some constant speed V. There are *N* number of agglomerates with different sizes, each containing M_n number of individual nano-particles. We assume steady, fully developed flow and that there is no particle flux through the upper boundary CD. $F_{f,n}$ is the frictional force due to each agglomerate sliding along the bottom and the total particle-sliding friction force is

$$\sum_{n=1}^{N} F_{f,n} = \sum_{n=1}^{N} C_f * R_n = \sum_{n=1}^{N} C_f \left(F_{g,n} - F_{e,n}\right), \qquad (4.9)$$

where C_f is the coefficient of friction (assumed to be a constant), R_n is the reaction force, $F_{g,n}$ is the gravitational force and $F_{e,n}$ is the electrostatic repulsion force associated with each agglomerated particle. Since the agglomerates each contain M_n number of individual nano-particles, $F_{g,n} = \sum_{m=1}^{M_n} F_{g,m}$ and $F_{e,n} = \sum_{m=1}^{M_n} F_{e,m}$ where $F_{g,m}$ and $F_{e,m}$ are the gravitational and electrostatic forces associated with each primary nano-particle, respectively.

From the momentum conservation in x direction, it is found that

$$\left(p_1 - p_2\right)A = F_v + \sum_{n=1}^{N} F_{f,n} = F_v + \sum_{n=1}^{N} C_f \left(F_{g,n} - F_{e,n}\right) \qquad (4.10)$$

where F_v is the viscous force for the fluid flow.

Substitution of the expressions for $F_{G,n}$ and $F_{E,n}$ yields

$$\left(p_1 - p_2\right)A = F_v + C_f \sum_{n=1}^{N} \sum_{m=1}^{M_n} \left(F_{g,m} - F_{e,m}\right) \qquad (4.11)$$

As the mass loading ratio (the concentration level) of the aerosol increases, the number of agglomerates, *N*, or the size of the agglomerates increases (Fig 8). An increase in the agglomerate size means an increase in the number of nano-particles, M_n. For both cases, when the magnitude of $F_{e,m}$ is smaller than that of $F_{g,m}$, the pressure difference $\left(p_1 - p_2\right)$ must be increased in order to sustain the conveying of the agglomerates. This leads to a higher conveying-air velocity and therefore a higher Froude number, as was observed in the transport of carbon-black nano-particles, micron-sized

glass beads and other particles. However, if the magnitude of $F_{e,m}$ is comparable to that of $F_{g,m}$, it is clearly seen that the friction term, $\sum_{n=1}^{N} F_{f,n}$, will be nearly cancelled, making the pressure difference $(p_1 - p_2)$ nearly independent of the number of agglomerates or independent of the agglomerate size. In this way, the Froude number can be independent of mass-loading ratio, a result which was observed with silica nano-particles. In conclusion, it is believed that the electrostatic-repulsion force effects the saltation of the silica nano-particles in such a way that the saltation Froude number does not increase with increasing mass-loading ratio.

The near cancellation of the friction term due to strong electrostatic forces would seem to imply that the agglomerates should continue their travel at any pressure difference $(p_1 - p_2)$ and therefore saltation should never occur for nano-silica, an inference which contradicts the experimental results. The simple control-volume analysis above ignores the Van Der Waals forces as well as the effect of the impaction of the bouncing agglomerates on the pipe wall, both of which also reduces the particles' momentum. Therefore, even if the friction force is nearly canceled due to the electrostatic repulsive force, saltation can occur for nano-silica at some pressure difference $(p_1 - p_2)$ which is not high enough to re-accelerate the agglomerates that had lost some or all of their momentum through collisions and Van Der Waals interactions with the pipe wall.

Chapter 4

Conclusions

Plasynki's conclusion that the Matsumoto 1977 [3] correlation yields the best prediction is experimentally validated for 47.5 μm glass beads. Good qualitative agreement is seen between the experimental results and the correlations. Quantitatively, the discrepancy between the predicted values of Matsumoto 1977 [3] and the measured experimental values was 39.8% in terms of the root mean square of deviations (R.M.S of deviation) of the Froude numbers, which is consistent with the discrepancy calculated by Plasynski [6].

The saltation of silica and carbon-black nano-particle aerosols was different than that of 47.5 μm glass beads in terms of the form and the initial position of the particles that settle. Large agglomerates of nano-particles were observed to slide and then settle at the bottom of the pipe, whereas, for micron-sized glass beads, the settling particles were the individual beads which were suspended in the conveying air before settling

The saltation Froude numbers predicted by Matsumoto 1977 [3] are an order of magnitude higher than the experimental results for nano-particles. By the calculating the forces acting between two particles, it is found that comparing the Matsumoto correlation and the experimental results for nano-particle aerosols is not reasonable since the Matsumoto comparison is based on Froude number which considers gravitational and inertial forces, whereas the thermal, electrostatic and Van Der Waals forces become more significant than gravitational forces for nano-particles.

The saltation of the silica nano-particles was different than that of carbon black nano-particles in such way that the saltation Froude number was independent of mass loading ratio. By measuring the charge level of the aerosols, it is found that the nano-silica aerosol had high negative charge. As a result of the control-volume analysis of the agglomerates traveling the bottom of the pipe, it is believed that the electrostatic-repulsion forces between the agglomerates and the pipe surface is the reason for the different saltation behavior of the silica nano-particles.

Chapter 5

Future Work

In order to compare the experimental results with the Matsumoto 1977 [3] correlation, the agglomerates that slide at the bottom of the pipe and form dunes should be characterized in terms of their size and their mass feed rate. Even if they are characterized, since the Matsumoto correlation is based on narrow particle-size distributions and the agglomerates are believed to have wide particle-size distributions, it is possible that there would be considerable difference between the experimental and the predicted values.

Most importantly, the link between the agglomerates' characteristic values and the initial aerosol characteristic values must be found in order to devise a predictive correlation for the saltation velocity of nano-particles. Since it is obvious that agglomeration is important regarding the saltation of the nano-particles, the mechanisms that lead to agglomeration must be investigated. One likely mechanism is the coupled Brownian and turbulent coagulation of the nano-particles and their agglomerates. This coupled mechanisms cause the size and mass-feed rate of the agglomerates bouncing and sliding along the bottom of the pipe to depend on parameters such as: the size and the mass-feed rate of the aerosol entering the pipe, and the residence time of the aerosol inside the pipe(which is related to the length of the pipe, the diameter of the pipe and the velocity of the conveying air). Another mechanism would be the deposition of the aerosol on the pipe wall and its detachment in the form of agglomerates which might be based on some or all of the previously mentioned parameters. The nature and the relative

significance of agglomeration mechanisms must be investigated so that the relationship between the agglomerates' characteristics and the system parameters can be found in order to devise a fully predictive correlation for the saltation velocity of nano-particles.

Appendix A

The particles are collected in a HEPA filter connected to the end of the conveying pipe. The air-tight filter housing which is described below contains and connects the filter to the pipe.

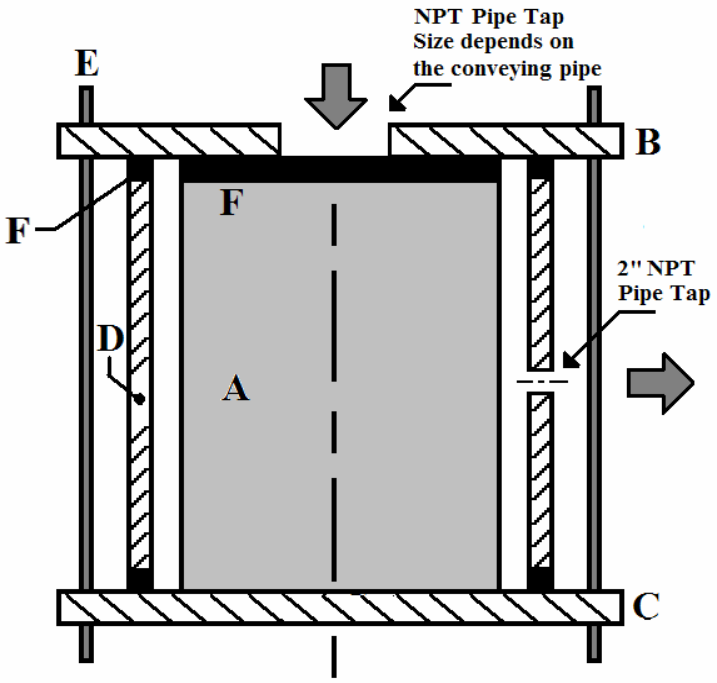

Figure 16: The schematic of the HEPA filter and its housing.

The filter, **A**, is a cylindrical shop-vac filter with a closed bottom surface that has a diameter of 7.5 in. and a height of 7 in., approximately. The filters bottom surface is closed. The air is introduced from its top surface and is filtered through its lateral surface which is made of HEPA filter medium. The upper and lower plates **B** and **C** have the same diameter of 12 in. and a thickness of 0.5 in. and they are used to compress the filter and the housing **D** via threaded rods **E**. To aid the compression and to prevent leakage, O-rings with square cross-sections, **F**, are attached to the top surface of the filter and also

to the top and bottom surfaces of the housing. The plate **B** is made out of acrylic which makes it possible to observe the filling of the filter and it is also tapped in the center where it is connected to the conveying pipe which is threaded at the end. This way, the pipe is directly connected to the filter without any end effects. The housing, **D** is made out of a 8 in. plastic pipe with a wall thickness of 0.34 in. and it has a ½ in. tapped hole on its lateral surface for the outlet of the filtered air. A barbed pipe fitting is connected to this hole in order to introduce the filtered air to the rotameter via tygon tubing.

Appendix B

SAG 410/H high flow rate aerosol generator (Topas-Gmbh) creates the aerosol by utilizing dry dispersion technique. The powder is metered to an ejector nozzle by a moving toothed belt and the well defined spaces between the teeth enables a stable volume feed rate of the powder. The volume feed rate is adjusted by changing the speed of the feed belt which is displayed in percentage values on the control panel. The powder is picked up from the belt by an ejector nozzle and the shear forces created in the ejector nozzle disperse the powder. The powder is filled into a vessel, where a scraper is located in order to fill the spaces between the teeth of the belt. The scraper eliminates the effect of powder level in the vessel on the powder bulk density and therefore on the powder mass feed rate. Since mass flow-rate of the powder depends not only on the belt speed but also on the powder bulk density, SAG 410 must be calibrated for every new powder to be tested if the powder bulk density is not known.

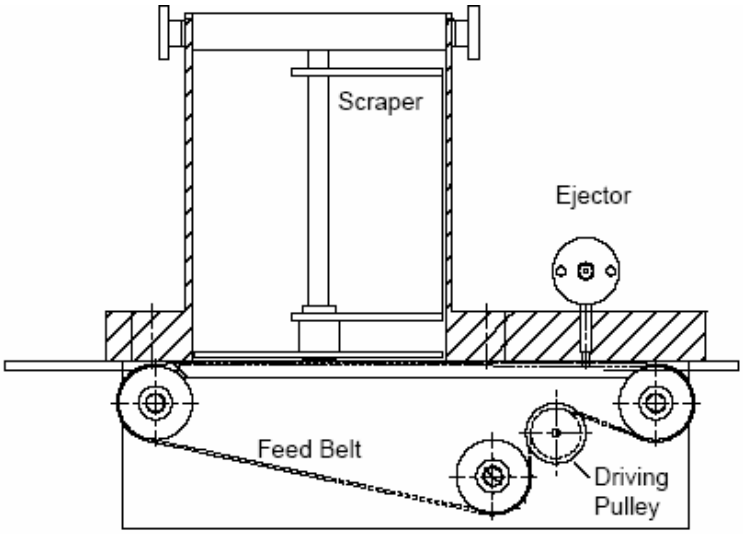

Figure 17: The schematic of the SAG 410

The calibration is done by blowing the powder into the HEPA filter described previously and measuring the differential mass on filter at different belt speed values for a given time interval.

The calibration curve results for glass beads, silica nano-particles, Carbon Black 50% and 100% are shown in the figures below.

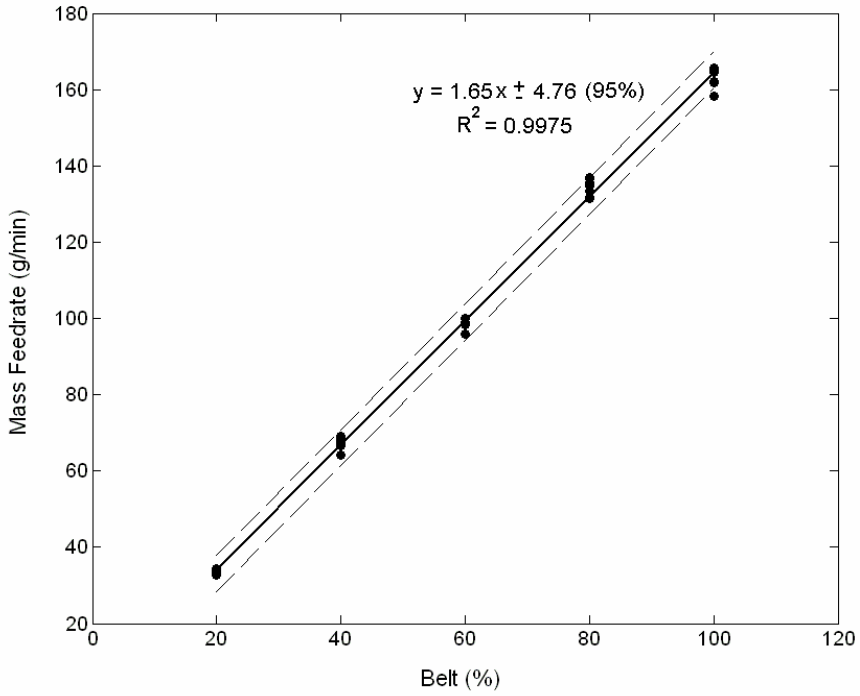

Figure 18: The mass feed rate curve of glass beads at different belt speed values with its 95% confidence interval.

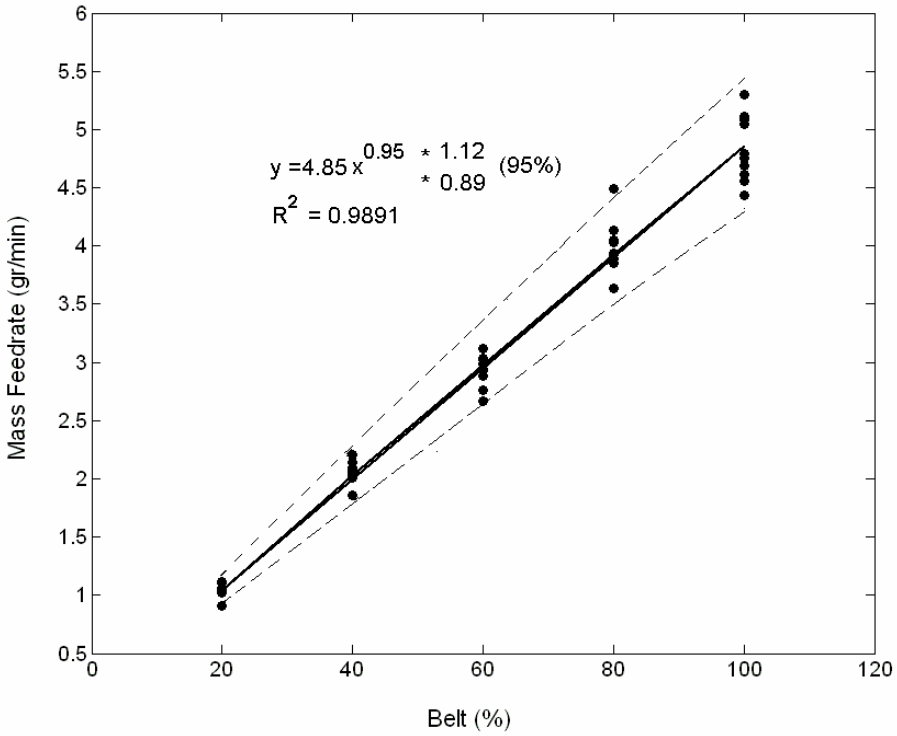

Figure 19: The mass feed rate power curve of silica nano-particles at different belt speed values with its 95% confidence interval.

Due to the increasing scatter of data at higher belt speeds, the mass feed rate curve of nano-silica is taken to be a power curve, since its confidence interval accommodates the scatter better than a linear fit can.

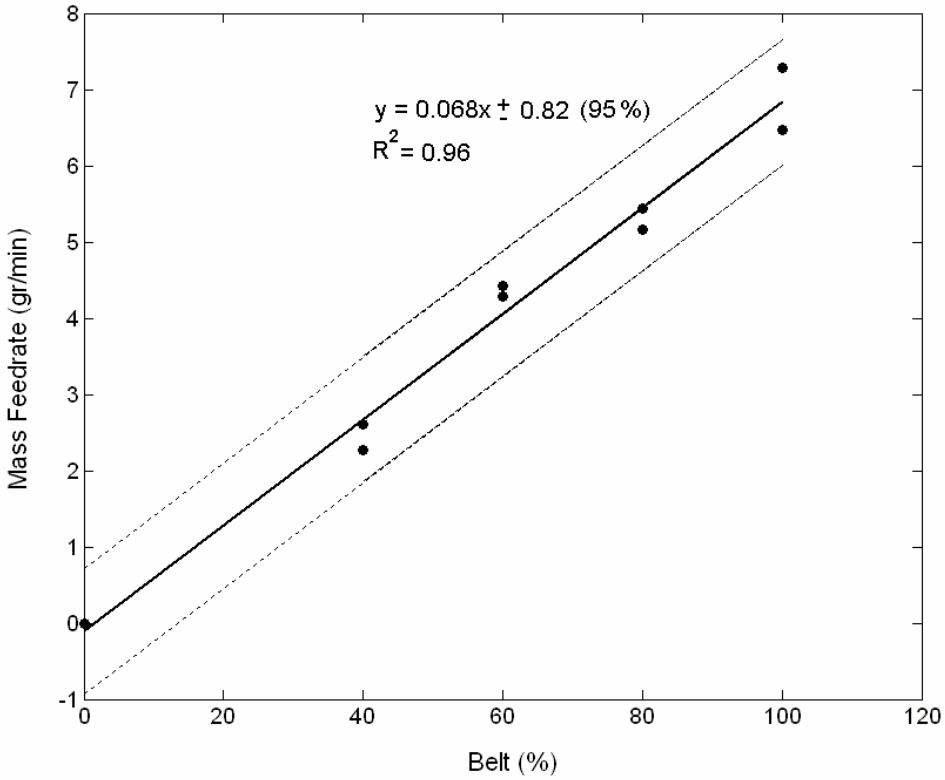

Figure 20: The mass feed rate curve of carbon black 50% nano-particles at different belt speed values with its 95% confidence interval.

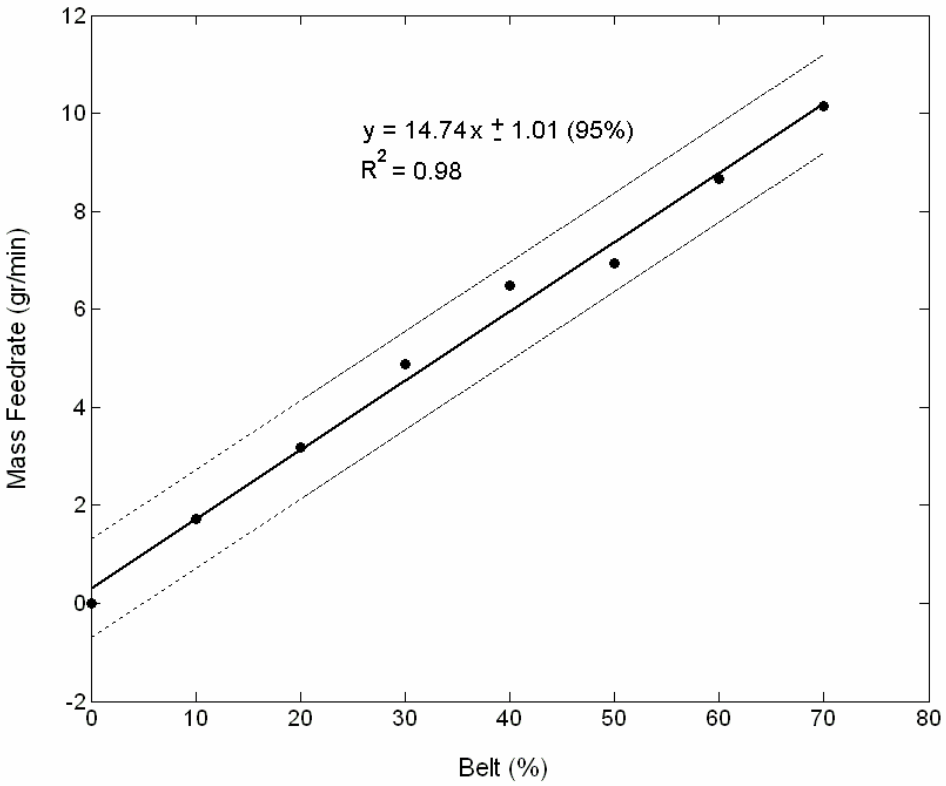

Figure 21: The mass feed rate curve of carbon black 100% nano-particles at different belt speed values with its 95% confidence interval.

Appendix C

In order to characterize the agglomerated particles sliding and bouncing at the bottom of the pipe, their pictures were taken with the camera Megaplus E.S 1.0 from the bottom of the bottom with a distance of 13.6 in.. The particles were illuminated from the top of the pipe. Micro-NIKKOR lens (Nikon USA) with a focal length of 105 mm was used and for the given distance it yielded a field of view size of 30/32 in. to 30/32 in. and a pixel size of 24 μm. From the preliminary pictures taken, it was understood that there was considerable particle overlap in the images once the bouncing particles were also included in pictures. To avoid this overlap, the field of depth should be set thinner so that the camera will focus and capture only the particles sliding at the bottom of the pipe. Therefore, the minimum f-stop value of f/2.8 was used which yields a field of depth value of 0.17 in. (4.3 mm) behind object. The measurements were based on the assumption that the sample taken from the sliding particles only would also represent the size distribution of the whole set of bouncing and sliding particles.

The pictures are taken for different mass loading ratios and are shown in Fig 9 of the Results and Discussion section.

In order to reduce the background noise caused by the non-uniform background illumination and by the particle residues on the surface of the pipe, the background images were subtracted from the particle images. The resulting particle pictures were converted into binary formats not only by threshold values that are manually set but also by threshold values automatically calculated by MATLAB Image Processing Toolbox. The processed images of Fig. 9a are shown in the figures below.

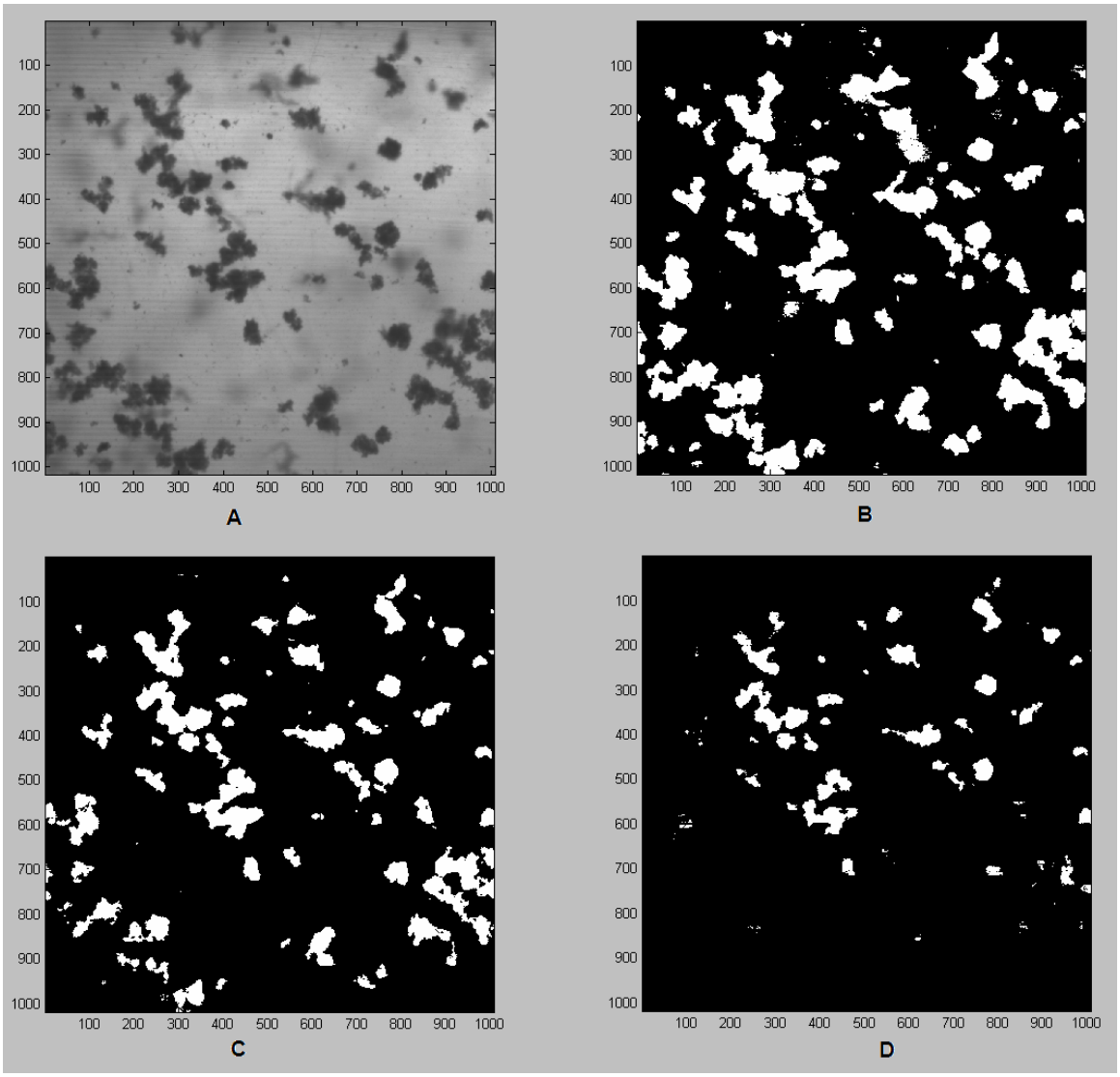

Figure 22: A) The agglomerates sliding at the bottom of the pipe at a mass feed rate of 2.98gr/min **B)** The corresponding binary image with the threshold value of 0.211 which is automatically set by MATLAB **C)** Binary image with the manually set threshold of 0.3 **D)** Binary image with the manually set threshold of 0.4

From the pictures above, it can be seen that there were 2 problems associated with the binary particle images in terms of determining the size distribution.

Firstly, in the original image it is believed that there are overlaps of several individual agglomerates. When these overlapped agglomerates are converted into their

binary format, as can be clearly seen in Fig. B, their structures merge and they are computed as a single large structure, which results the overestimation of particle mean size in the statistical analysis done by MATLAB Image Processing Toolbox. However, this problem can be partially solved by manually increasing the threshold value as can be seen in Fig. C and D. On the other hand, it should be noted that increase in the threshold value might lead to the shrinkage or even the elimination of some of the binary structures, a problem that can be seen clearly in Fig. D.

Secondly, most of the bouncing particles were out of focus and therefore they were captured as blurry images in the pictures. When these blurry images were converted into binary format, depending on their sharpness and the threshold value chosen, some of them were split into many small binary structures while others were converted to large structures that didn't have well defined boundaries, boundaries that have extensions of many small binary structures. For both cases, small structures were introduced into the binary image, leading to significant shift in the particle size distribution. The resulting particle area histograms of binary images with different threshold values are shown below.

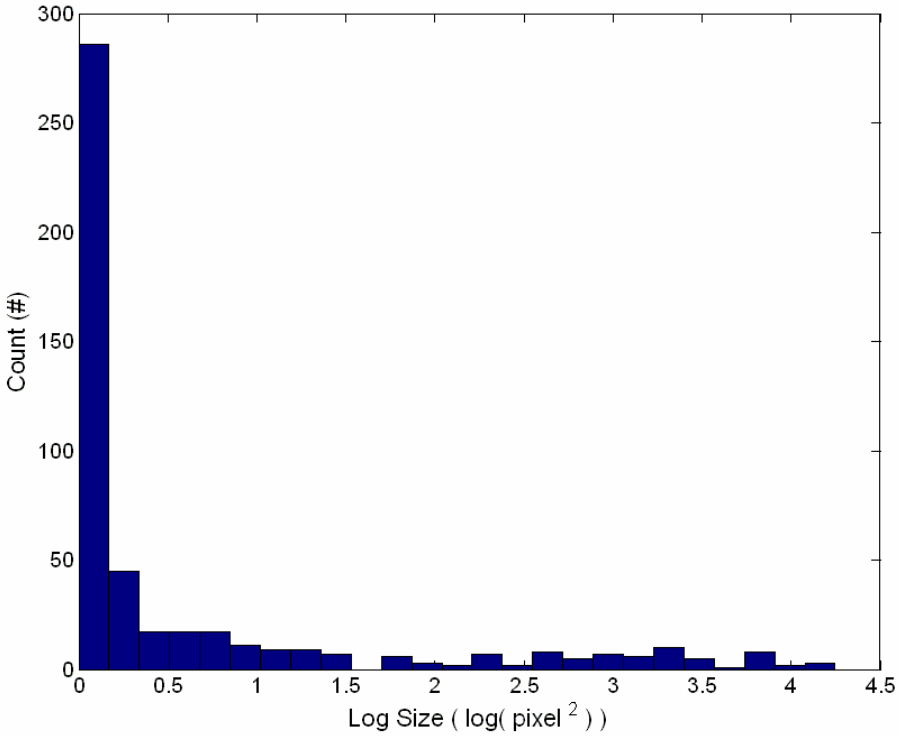

Figure 23: The size histogram of the binary image with the threshold value of 0.211.

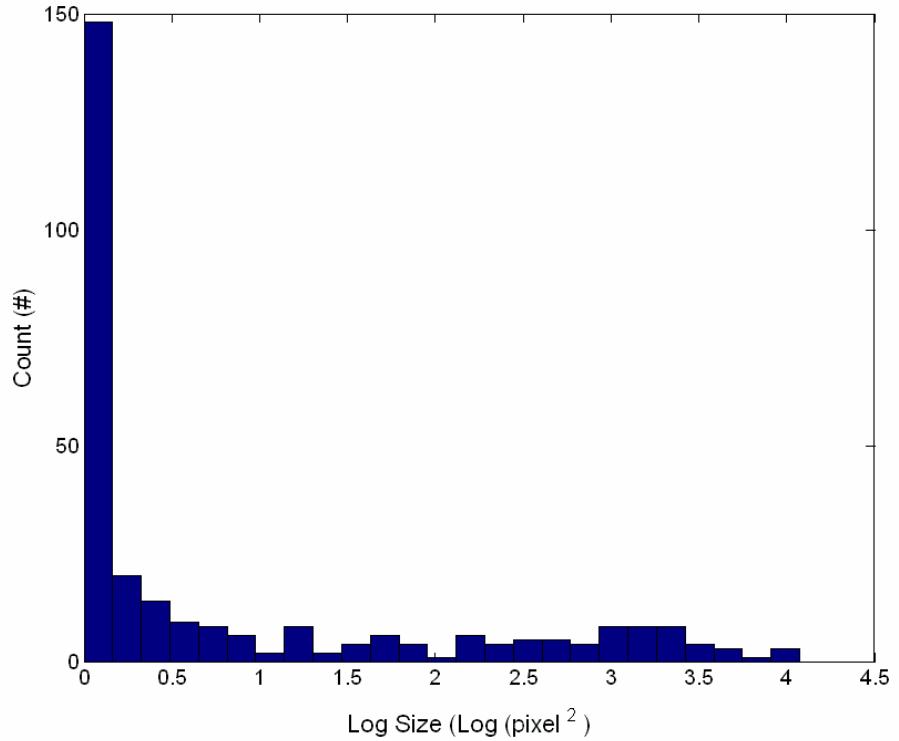

Figure 24: The size histogram of the binary image with the threshold value of 0.3.

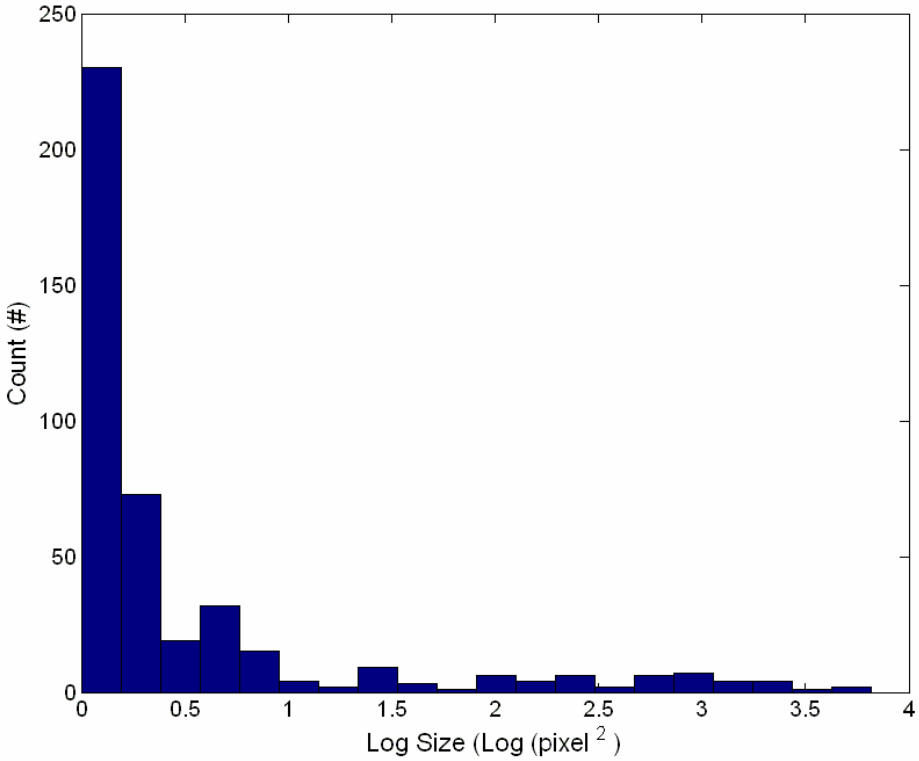

Figure 25: The size histogram of the binary image with the threshold value of 0.4.

As can be seen from the pictures, all of the logarithmic histograms have a peak at a logarithmic area value of 0, which corresponds to 1 pixel^2. Additionally, the total number of structures that have sizes between 2 pixel^2 and 5 pixel^2 are higher than the total number of larger structures. It is believed the large number of smaller structures is due to inaccurate binary conversion of the blurry images of the bouncing particles that were out of focus.

Therefore it is concluded that, the particle imaging technique used does not result an accurate size distribution measurement of the particles sliding at the bottom of the pipe.

Appendix D

In order to measure the mass feed rate of the agglomerates sliding and bouncing at the bottom of the pipe, a tool that splits the flow and collects the agglomerates was devised. The schematic of the tool is shown in the picture below.

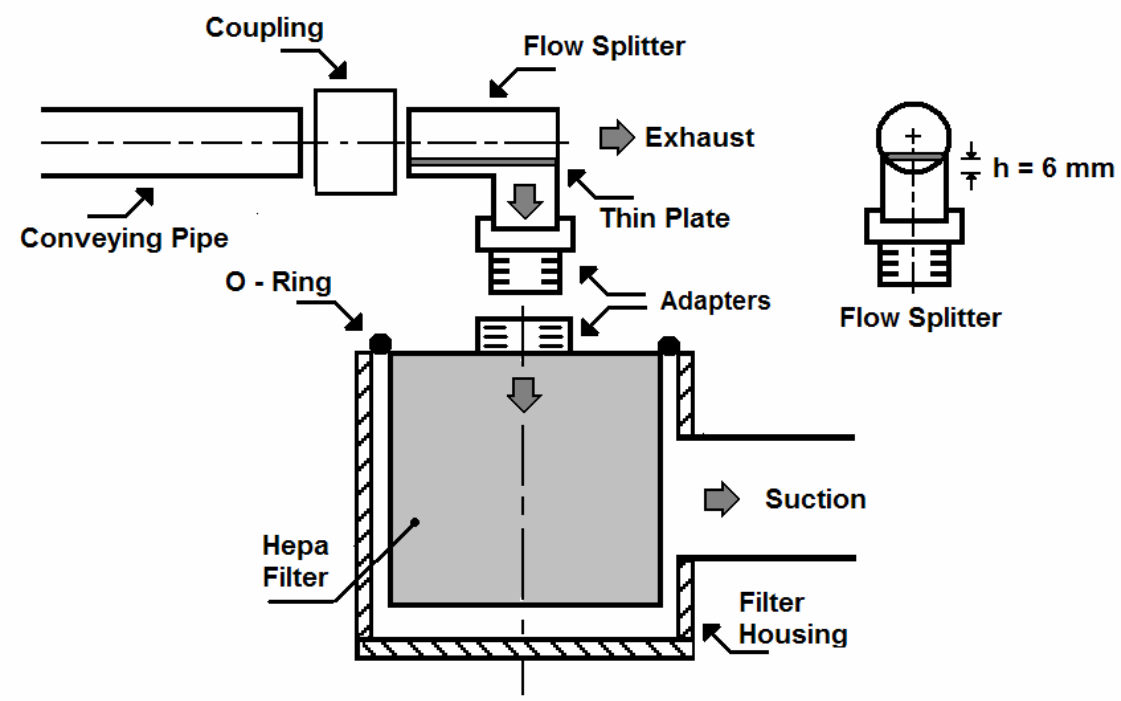

Figure 26: The flow splitter and its location in the system.

The flow splitter is basically a clear PVC pipe elbow that contains a thin metal plate that splits the flow. It is connected to the conveying pipe with a pipe coupling. The portion of the flow that goes over the thin plate contains mainly small particles and it is exhausted through the open end of the splitter. The bottom portion of the flow which contains the sliding and bouncing agglomerates goes through the thin channel which is

formed by the thin plate and bottom surface of the flow splitter and it is directed into the HEPA filter (Appendix A) for collection. The HEPA filter is connected to the flow splitter though pipe adapters.

Because of the pressure drop across the filter, the flow within the thin channel wasn't strong enough to convey the sliding and bouncing agglomerates and transport them into the filter. Therefore suction was utilized in order to increase the flow through the channel and convey the agglomerates into the filter. In order to maximize the suction, the HEPA filter is confined within an 8 in. PVC pipe which is connected to the suction duct through a hole on its lateral surface. The bottom surface of the 8 in. PVC housing is capped and the top surface is sealed with an O-ring in order to prevent leakage.

The thickness of the channel that transports the sliding and bouncing particles into the filter is taken to be 6mm which is based on the pictures of the agglomerates. The pictures are taken with the Megaplus E.S 1.0 camera which is synchronized with a pulsed laser sheet that is perpendicular to the direction of the flow. The laser sheet is placed right in the vicinity of the pipe exit and therefore it illuminates not only the particles but also the surface of pipe end. The camera was leveled with the pipe and it was oriented with a 45^{o} angle to the direction of the flow. From the images of the agglomerates and the pipe cross section, it was possible to measure the maximum height that the bouncing particles can reach up to. The thickness of the channel is based on this maximum height is determined to be 6 mm. The picture from which the separation height is determined is shown in Figure 27:

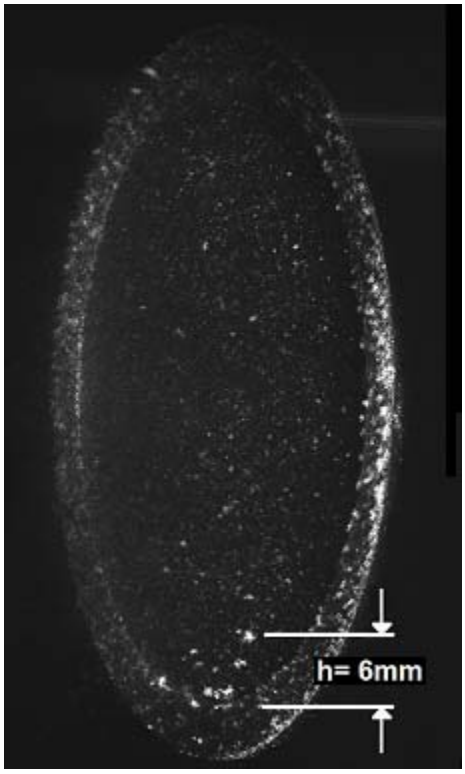

Figure 27: The image used to determine the height of the thin plate which is used to split the flow.

The differential mass of the filter over measured time intervals yields the mass feed rate of the agglomerates. After several runs, it was concluded that the flow splitter was able to function without any problem and it was possible to determine the mass feed rate of agglomerates sliding and bouncing at the bottom of the pipe.

Appendix E

Isokinetic sampling ensures that a sample taken from a moving aerosol stream represents the aerosol accurately, in terms of the concentration and size distribution. Sampling is isokinetic when the inlet axis of the probe is aligned with the direction of the aerosol flow and the gas velocity entering the probe is equal to the free-stream velocity approaching the probe. This way there is no distortion of the streamlines and therefore no particle loss due to particle inertia. Anisokinetic sampling which is a failure to achieve isokinetic sampling, results biased measurements of the mass concentration and particle size distribution. Depending on the conditions, the sample may contain an excess or deficiency of large particles. The following figures illustrate the three different conditions of anisokinetic sampling.

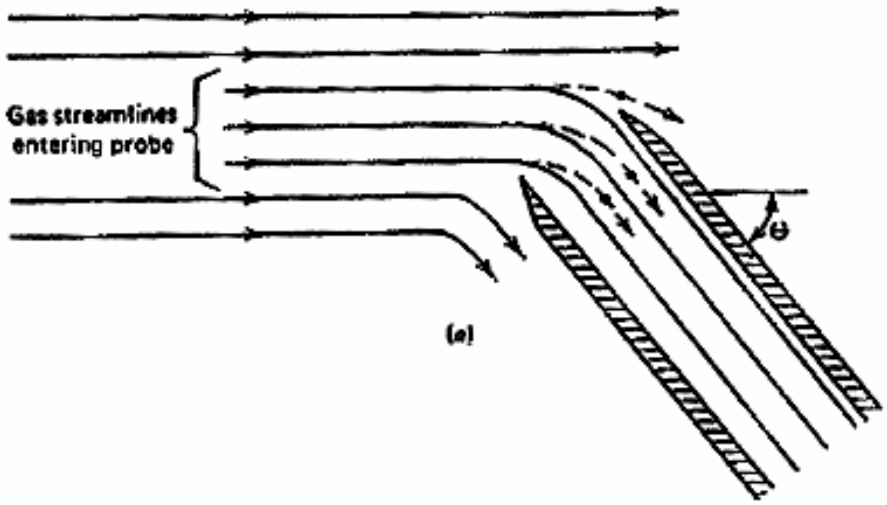

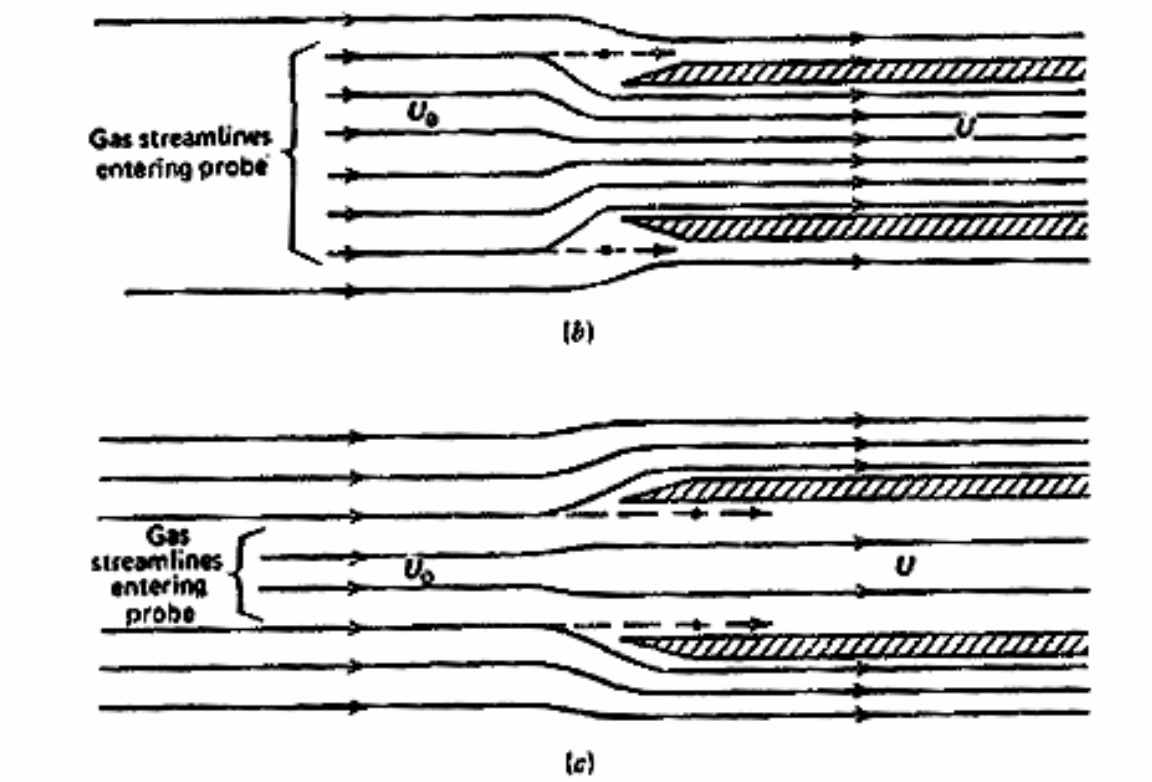

Figure 28: Anisokinetic sampling a) Misalignment. $\Theta \neq 0$ b) Superisokinetic sampling $U > U_O$ c) Subisokinetic sampling $U < U_O$ [20]

In all of the conditions illustrated in the figure above, some of the large particles approaching the probe will not be able to follow the distorted streamlines because of their high inertia. If the probe is misaligned or the sampling is superisokinetic, the large particles will travel beyond the probe and will not be included in the sample, leading to a large particle deficiency in the size measurement. For subisokinetic sampling, the large particles that cannot turn quickly enough will be included in the sample, leading to an excess of large particles in the size measurement. Therefore, in order to measure the size distribution of an aerosol accurately, it is essential to align the probe with the direction of the flow and match the free stream with the sampling flow velocity.

The schematic of the experimental set-up used for sampling is shown in the figure below

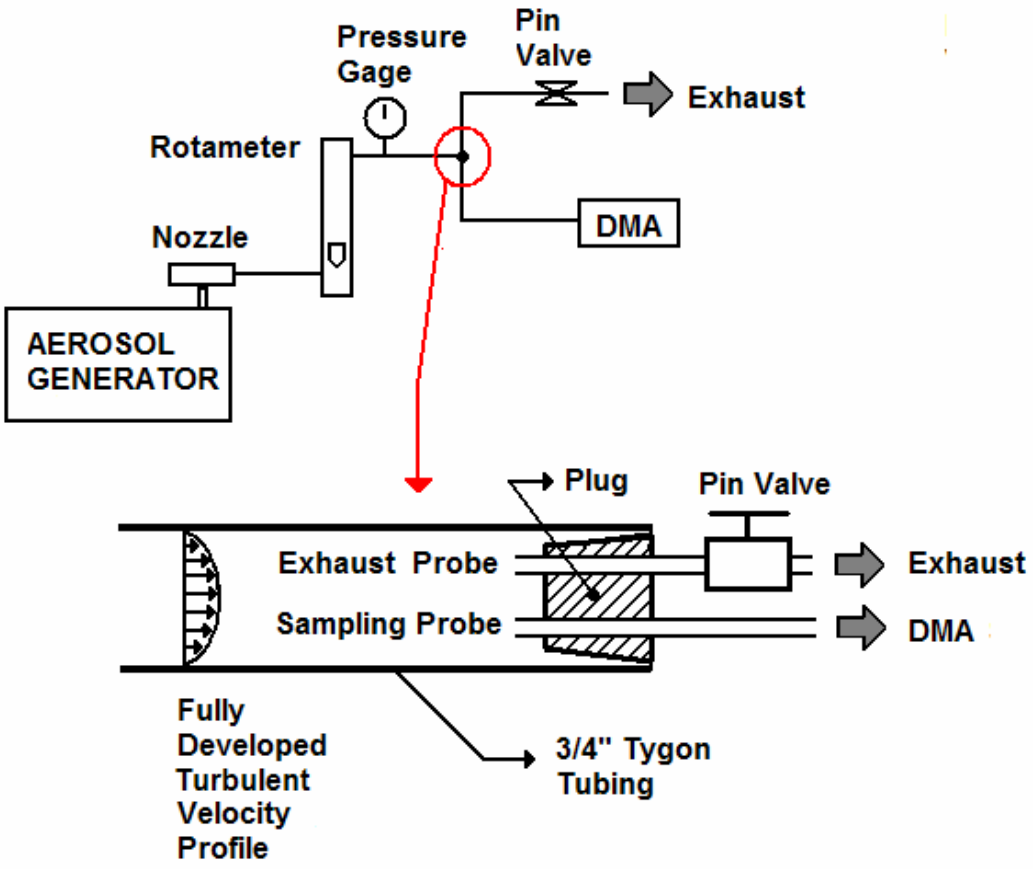

Figure 29: The schematic of the experimental used for iso-kinetic sampling.

Before introducing the particle laden flow into the system, the air free stream velocity is matched with the sampling flow velocity. The air exiting the nozzle goes through a rotameter which is connected to a pressure gage with a tee fitting. The pressure gage measures the back pressure and therefore enables the correction of the air flow rate measured by the rotameter. Downstream of the rotameter, the air flow splits into two directions: some of it goes into the 0.09 in. I.D. sampling probe and it is analyzed by the differential mobility analyzer (DMA) from TSI, which measures the size distribution of

the aerosol and the remaining air flow is exhausted though the exhaust probe. The plug connects the probes to the ¾ in. tygon tubing and aligns them with axis of the air flow.

The air flow in the tygon tubing is measured to be turbulent and its velocity profile is calculated on the basis of the power law: $V/U_{MAX} = \left(1-\frac{r}{R}\right)^{\frac{1}{n}}$ and $\frac{1}{n} = \sqrt{f}$ for f < 0.1 where f is the friction factor. Since the location of the sampling probe, r, the inner radius of the tygon tubing, R, and the air flow rate is known, the friction factor (f) and the velocity of the air approaching the probe, V_a, can be found by the power law formula. The sample flow rate is indirectly controlled by the pin valve and is measured by the differential pressure flow meter inside DMA. Since the probe I.D is known, the sample air velocity, V_s, can be calculated. By adjusting the pin valve, the isokinetic sampling is assumed to be achieved when V_a and V_s values are approximately equal to each other with a maximum discrepancy of 5%.

Once the velocities are matched, the rotameter is disconnected from the system and this time particle laden flow is introduced into the system by the aerosol generator with the same pin valve setting. The flow rate increases slightly since the rotameter is disconnected from the system. This increase is compensated by reducing the aerosol flow rate with the pressure regulator of the aerosol generator until the same sample flow rate value which was measured previously by DMA is reached again. This way, it is believed that the ratio of V_a to V_s stays in the 5% error limit.

Sampling is done for nano-particle aerosols of silica, carbon black 50% and 100% with the procedure explained above. The size distribution was measured up to a particle size of approximately 270nm for each aerosol, a limit which is imposed by DMA based

on the sample flow rates that are within the 5% isokinetic sampling error and also other parameters associated with the equipment.

References

1. Matsumoto, S., Hara M., Saito, S. and Maeda, S., Journal of Chemical Engineering of Japan,7, 425 (1974)

2. Wirth, K.E., Ger. Chem. Eng.,6 ,45 (1983)

3. Matsumoto, S., Kikuta M. and Maeda, S., Journal of Chemical Engineering of Japan,10, 4, 273 (1977)

4. Gunther, W., "Unterschungen Uber die Druckverluste in pneumatischen Forderletlungen und Beitrag zur Berechnung der Druckverluste mit besonderer Beracksichtigung des Fordervorganges im Behurrungszusland," Dissertation, TH Karlsruhe (1957).

5. Rizk, F., "Pneumatic conveying at optimal operating conditions and a solution of barth's equation $\lambda_z = \varphi(\lambda_z, \beta)$," Proc. Pneumotransport 3, Paper D4, Bath, England (1976)

6. Plasynski, S., Dhodapkar, S., Klingzig, G. E., Cabrejos, F., Comparison of saltation velocity and pickup velocity correlations for pneumatic conveying, AIChE Symp. Ser. 87 (1991) 78-90.

7. Shi, H., Kleinstreuer, C., Zhang, Z., Kim, C. S., "Nanoparticle transport and deposition in bifurcating tubes with different inlet conditions" Physics of Fluids, 16, 7, 2199 (2004)

8. Cohen, B. S., Asgharian, B., "Deposition of ultrafine particles in the upper airways: an empirical analysis", Journal of Aerosol Science, 21, 6, 789-797 (1990)

9. Ingham, D. B., "Diffusion of aerosols in the entrance region of a smooth cylindrical pipe", Journal of Aerosol Science, 22, 3, 253-257, (1991)

10. Martonen, T., Zhang, Z. and Yang, Y., "Particle diffusion with entrance effects in a smooth-walled cylinder", Journal of Aerosol Science, 27, 1, 139-150 (1996)

11. Otani, Y., Namiki, N. and Emi, H., "Removal of fine particles from smooth flat surfaces by consecutive pulse air jets", Aerosol Science and Technology, 23, 665-673 (1995)

12. Wen, H. Y, Kasper, G., "On the kinetics of particle re-entrainment from surfaces", Journal of Aerosol Science, 20, 4, 483-498 (1989)

13. Wen, H. Y, Kasper, G., and Udihas, R., "Short and long term particle release from surfaced under the influence of gas flow", Journal of Aerosol Science, 20, 923-926 (1989)

14. Hinkle, B.L. -- 1953 PhD Thesis, Georgia Institute of Technology

15. Hinds, W. C., "Aerosol Technology", John Wiley & Son, Inc., New York, 1999, p86

16. Hinds, W. C., "Aerosol Technology", John Wiley & Son, Inc., New York, 1999, p336

17. Hinds, W. C., "Aerosol Technology", John Wiley & Son, Inc., New York, 1999, p151

18. Hinds, W. C., "Aerosol Technology", John Wiley & Son, Inc., New York, 1999, p316

19. Lowell J., Journal of Physics D: Applied Physics. 23 1082-1091 (1990)

20. Hinds, W. C., "Aerosol Technology", John Wiley & Son, Inc., New York, 1999, p208